In-Context Learning for Wound Classification with Small Multimodal Language Models

George Martvel[1@], Oskar Gustafsson[2,3], John Pavia[3], Ernst Ahlberg[3,4]

[1]Jönköping University, Jönköping, Sweden
[2]Halmstad University, Halmstad, Sweden
[3]Mölnlycke Health Care
[4]Centre for Reliable Machine Learning, Royal Holloway, University of London, Egham, Surrey, UK

[@]Corresponding author: georgy.martvel@ju.se

arXiv:2607.18819v1 [cs.CV] 21 Jul 2026

Abstract

Background and Objective: Wound image classification is often treated as a task-specific supervised learning problem, requiring substantial amounts of manually labelled data and retraining when the label space or deployment setting changes. This study evaluated whether small multimodal language models (SMLMs) can provide a training-free alternative for wound classification through retrieval-based in-context learning (ICL).

Methods: Experiments used two public wound-image datasets: the Kaggle wound dataset (1469 images, 10 classes) and the Medetec dataset (560 images, 9 classes). Eleven SMLMs from the Qwen 3.5, Ministral 3, and Gemma 4 families were evaluated under zero-shot prompting and few-shot prompting with random support examples, embedding-based k-nearest-neighbour (kNN) retrieval, and kNN retrieval followed by maximal marginal relevance reranking (MMR). Retrieval-only weighted-kNN controls, support-set reduction experiments, and support-context size sweeps were used to assess the effects of retrieval, model scale, and prompt length.

Results: Query-conditioned ICL consistently outperformed zero-shot and random few-shot prompting. On the Kaggle dataset, the best result was achieved by Qwen 3.5 27B with kNN+MMR, reaching 0.872 accuracy and 0.871 F1 score. On Medetec, Qwen 3.5 27B with kNN+MMR reached 0.678 accuracy and 0.670 F1. Larger models exceeded matched weighted-kNN controls, indicating use of retrieved examples beyond nearest-neighbour voting. Retrieval-based ICL degraded modestly under support-set reduction, and most gains saturated with 8–10 support images.

Conclusions: Retrieval-based ICL allows SMLMs to perform adaptable wound image classification without task-specific retraining. Compact retrieved contexts may support practical and privacy-conscious deployment, although performance remains dependent on model scale, retrieval strategy, and dataset difficulty.

1 Introduction

Computer vision is playing an increasingly important role in medical imaging [3], yet many high-performing systems still follow a task-specific paradigm: a dataset is collected and annotated for a single objective, a dedicated model is trained or fine-tuned, and the process is repeated whenever the task definition, label set, or deployment context changes [12, 31]. Although this approach can yield strong performance, it also requires substantial annotation effort and computational resources, particularly in settings where expert labels are scarce or practical requirements evolve rapidly [73]. Recent advances in large multimodal language models (LMLMs) suggest an alternative

to conventional supervised learning [14, 52, 66, 69]. Modern LMLMs can be applied in a zero-shot setting, in which the model receives only task instructions at inference time and requires neither annotated training data nor task-specific fine-tuning [40, 42]. In practice, however, this approach often yields moderate to good performance, depending on the complexity and specificity of the task [35, 52, 65].

The performance of LMLMs on specific tasks can be improved through adaptation strategies such as fine-tuning and in-context learning (ICL) [4, 15, 42]. In fine-tuning, model parameters are updated using task-specific training data, either across the full model or through lighter-weight adaptation schemes, which can yield strong performance when sufficient annotations and computational resources are available [22, 34]. In contrast, in ICL, a small number of labelled examples are provided directly in the prompt at inference time rather than being learned through training [4, 23]. Such prompting-based approaches are especially appealing in medicine because they allow for rapid adaptation with minimal task-specific data and without requiring a separate training pipeline for each application [51, 53].

A further practical issue is the choice of model scale. In deployment settings, one often distinguishes between smaller models that can run locally on consumer or edge hardware and larger models that typically require server-side or cloud inference. This distinction is only approximate, since the boundary is continuously shifting with developments in hardware, model architecture, and optimisation methods such as quantisation, pruning, and distillation [44, 70, 78]. In this work, we use the term small multimodal language models (SMLMs) in a deployment-oriented sense, referring to models suitable for local or edge-based inference rather than defining the term by a fixed parameter threshold. This deployment distinction is closely linked to an expected performance tradeoff: scaling-law studies show that, within comparable model families, performance improves predictably with model size, data, and training compute. However, size alone does not determine performance, and smaller models can be competitive when they are better trained or optimised [33, 36]. Thus, even though larger models are attractive when maximum task performance is the main objective, the dependence on server-side inference can be difficult to justify in privacy-sensitive settings, such as internal documentation, governmental workflows, or medical records, where data cannot always be sent to external model providers because of confidentiality, regulatory, or data-governance constraints [2, 11, 85]. Locally deployable SMLMs are therefore a realistic alternative [28], but their usefulness depends on how much performance is lost relative to larger remote models, and whether that loss is acceptable for the intended application.

These concerns are particularly relevant for wound analysis and classification. Wound images are clinically sensitive, visually heterogeneous, and often collected under variable lighting, distance, body location, and image-quality conditions. Additionally, labels usually require wound-care expertise and may differ across classification tasks such as wound type, tissue composition, infection, or referral urgency [7, 13, 80]. This makes the combination of SMLMs and ICL especially attractive: local inference can reduce the need to transmit patient images to external servers, while in-context examples can specify the target label set and decision criteria at inference time without retraining a separate model for every wound-related task [8, 26, 28, 51]. In such a setting, the goal is not necessarily to show that SMLMs outperform or match the performance of larger remote models, but to test whether example-guided local models can provide a useful privacy-preserving compromise between task adaptability, computational cost, and classification performance.

In this work, we examine whether small multimodal language models can serve as a practical solution for wound classification when task-specific training data is limited. Using open wound-image datasets, we evaluate zero-shot and few-shot prompting across eleven models from the Qwen 3.5 [58], Ministral 3 [50], and Gemma 4 [29] families, covering a range of SMLM scales under a common prompting protocol. We compare three strategies for constructing the few-shot context: random

support sampling, embedding-based k-nearest-neighbour (kNN) retrieval, and kNN retrieval followed by maximal marginal relevance reranking (MMR). To separate the contribution of in-context learning from that of retrieval itself, we also compare each retrieval-augmented prompting condition against a matched retrieval-only weighted-kNN baseline. Finally, we examine how progressively reducing the support/training set degrades the accuracy of retrieval-augmented prompting methods and conventional supervised classifiers, and evaluate how the size of the support context (number of support images) affects the performance of SMLMs.

2 Related Work

Prior research on wound image analysis has predominantly framed the task as a supervised computer vision problem, focusing on wound classification, detection, segmentation, tissue analysis, and measurement, usually with models trained for a specific wound-related endpoint and evaluated on a fixed label space [7, 71, 79, 80]. Earlier studies typically employed handcrafted colour, texture, or deep-feature representations with conventional classifiers [1, 79], while later work has moved toward CNN-based and deep ensemble methods for tasks such as infection, ischaemia, or wound-type classification [5, 30, 61]. A parallel line of work focuses on wound localisation, segmentation, and measurement, including tissue segmentation [60, 62, 71, 72]. Multimodal wound classification models have also been proposed, for instance by combining wound images with anatomical location information; however, these approaches still operate within a supervised learning framework and require training for predefined tasks [6, 56]. Similarly, work on surgical wound infection assessment and postoperative monitoring has mostly focused on models designed for a specific clinical endpoint, such as identifying infection risk from wound images, patient-reported symptoms, or other structured inputs [13, 46, 76]. Overall, the existing literature demonstrates that image-based wound assessment is an active research area, but it remains dominated by task-specific supervised systems.

Large language models and foundation models provide a possible way to move beyond fully task-specific wound-analysis pipelines. In medical imaging, recent surveys discuss pretrained models as reusable backbones for transfer learning, domain adaptation, and annotation-efficient learning [9, 81]. Some studies have tested whether general-purpose visual representations transfer to medical images: for example, DINOv2 [54] has been evaluated on radiology benchmarks using settings such as kNN classification, few-shot learning, linear probing, and fine-tuning, showing that natural-image pretraining can provide useful features for some medical tasks [10]. Vision–language models represent a significant development in this area, as exemplified by CLIP, which introduced shared image–text embeddings that support zero-shot classification and image retrieval [59]. Biomedical variants of CLIP, such as PubMedCLIP, MedCLIP, and BiomedCLIP adapt this idea to medical image-text data [25, 74, 82]. For wound classification, this suggests that both general and medical-pretrained image or image-text representations may be useful when wound-specific annotations are limited.

A related line of work investigates whether pretrained multimodal models can be adapted through examples at inference time (in-context learning). Med-Flamingo was one of the earliest multimodal models developed specifically for medical applications, showing that few-shot multimodal prompting can be used for medical visual question answering [51]. Later work tested the same idea in more diagnostic classification settings. Ferber et al. showed that in-context examples improve GPT-4V performance on cancer histopathology tasks and can reach the level of specialist classifiers in some settings [26]. Similar evidence has been reported in ophthalmology: Ayhan et al. reported that Gemini 1.5 Pro with ICL achieved diabetic retinopathy detection accuracy

and F1 scores close to a supervised algorithm [8], and Choi and Yoo demonstrated that example-based prompting improved GPT-4o performance across several ophthalmic image-interpretation tasks [18]. In recent oncology work, Shrestha et al. compared several large multimodal language models under ICL across datasets such as MHIST, PatchCamelyon, and HAM10000, showing consistent gains from few-shot prompting while also indicating that fully fine-tuned systems still represent a strong ceiling [63]. These studies suggest that ICL can be useful in medical contexts when only a small number of labelled examples are available. However, the evidence is drawn primarily from pathology, oncology, and ophthalmology, and many studies rely on large externally hosted models.

Smaller model scales are particularly advantageous for wound classification. Wound images may be collected in hospitals, outpatient clinics, or home-care settings, and they often contain sensitive clinical information. In such cases, sending images to an external model provider may be challenging because of privacy constraints [85]. Smaller models are therefore relevant not only because they are cheaper or faster, but because they can be run locally. Surveys of small and on-device language models describe these models as useful for lower-cost, lower-latency, and resource-constrained deployment [44, 70, 78], and similar arguments have been made for small language models in healthcare [28]. At the same time, local deployment is useful only if the performance loss is acceptable.

Few-shot prompting (or in-context learning) may benefit smaller models by providing task-specific information without fine-tuning or remote inference, but it raises another practical question: which examples should be shown to the model? In visual and multimodal ICL, performance can depend strongly on the selected examples, their order, and the retrieval strategy used to construct the prompt [17, 41, 45, 83]. If the support examples are poorly matched to the query, the model may receive little useful task information, and if they are too similar to each other, the prompt may contain repeated evidence rather than a useful coverage of the class variation. A common solution is retrieval-based selection, where the support examples are chosen by nearest-neighbour search in an embedding space, often using a visual or vision-language encoder such as CLIP [59]. Such retrieval-based strategies have been shown to improve over random example selection in visual ICL and are also used in multimodal ICL systems such as RICES [4, 45, 83]. However, nearest-neighbour retrieval remains a limited criterion: it can select examples that are redundant, overly prototypical, or similar to the query for reasons irrelevant to the target class. This is especially important in fine-grained image tasks, where small visual differences may define the label. Recent work, therefore, explores support-selection strategies that go beyond simple similarity, including diversity-aware context search, learned retrievers, and counterfactual or contrastive example selection [37, 39, 67, 77].

3 Methods

3.1 Ethics statement

This study does not include confidential information. All research procedures were conducted exclusively on publicly accessible, anonymised patient data, in compliance with all relevant ethical standards.

3.2 Problem definition

Let $\mathcal{D} = \{(I_j, y_j)\}_{j=1}^{N}$ denote an image corpus, where I_j is an image and y_j is its class label, belonging to a set of dataset labels $\mathcal{Y}$. To evaluate classification performance, $\mathcal{D}$ is divided into a support set $\mathcal{D}_{\text{sup}}$ and an evaluation set $\mathcal{D}_{\text{eval}}$. Given a query image $I_q \in \mathcal{D}_{\text{eval}}$, we construct

a prompt $\mathcal{P}_q$ containing the query image and task text. Optionally, the prompt also includes a retrieved support context $\mathcal{R} \subseteq \mathcal{D}_{\text{sup}}$. The multimodal model Φ then predicts a class label $\hat{y}_q$ from this input. Inference can therefore be written as

$$\hat{y}_q = \Phi(\mathcal{P}_q, \mathcal{R}).$$

In the zero-shot setting, $\mathcal{R} = \varnothing$, whereas in the ICL setting, $\mathcal{R}$ contains a set of retrieved, labelled support examples. Following prior work on multimodal in-context learning [26, 77], we used embedding-based retrieval to construct this support context before passing it to the downstream classifier. Figure 1 provides an overview of the full ICL pipeline.

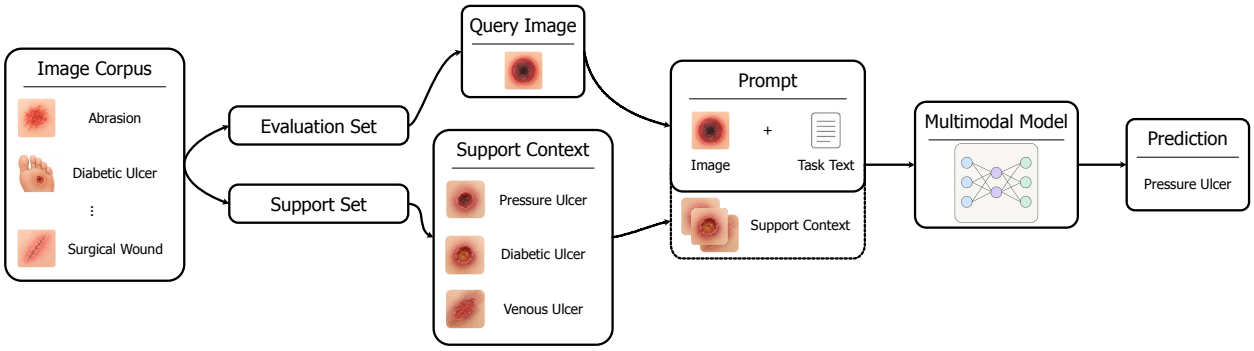

Figure 1: Schematic overview of the ICL pipeline used in the current study. The wound images were generated with OpenAI's GPT Image 2 for visual illustration only.

3.3 Datasets

Experiments were performed on two wound-image datasets. The first was the Kaggle dataset "Collected and Categorized Wound Images Dataset"[1], which comprised 10 classes: *Abrasions*, *Bruises*, *Burns*, *Cut*, *Diabetic Wounds*, *Laceration*, *Normal*, *Pressure Wounds*, *Surgical Wounds*, and *Venous Wounds*. Before defining the final splits, half of the images were removed as they were mirrored duplicates of existing samples. The resulting Kaggle wound image corpus comprised 1469 images and was divided into a support split and an evaluation split. The evaluation split was balanced, containing 25 randomly selected images per class and 250 images in total, while the support split contained the remaining 1219 images.

The second dataset was constructed from the Medetec Wound Database[2]. After excluding low-count categories (less than 15 images), the Medetec corpus contained 560 images across 9 classes: *Burns or Scalds*, *Diabetic Foot Ulcers*, *Extravasation Injuries*, *Infected or Necrotic Toes*, *Meningitis Skin Lesions*, *Miscellaneous*, *Orthopaedic Cases*, *Pressure Ulcers*, and *Venous or Arterial Ulcers*. As with the Kaggle dataset, the Medetec dataset was randomly divided into a support split and a balanced evaluation split. The evaluation set contained 10 images per class, for a total of 90 images; the remaining 470 images were used in the support set.

For both datasets, the support splits served as the retrieval pools for few-shot context construction, and the evaluation splits were kept fixed for model assessment. Figure 2 shows the class distributions for the Kaggle dataset (left) and the Medetec dataset (right).

[1] Ibrahim Fateen, *Collected and Categorized Wound Images Dataset*, Kaggle, `https://www.kaggle.com/datasets/ibrahimfateen/wound-classification` (accessed on 29 June 2026).

[2] Medetec, *Medetec Wound Database: stock pictures of wounds*, `https://www.medetec.co.uk/files/medetec-image-databases.html` (accessed on 29 June 2026).

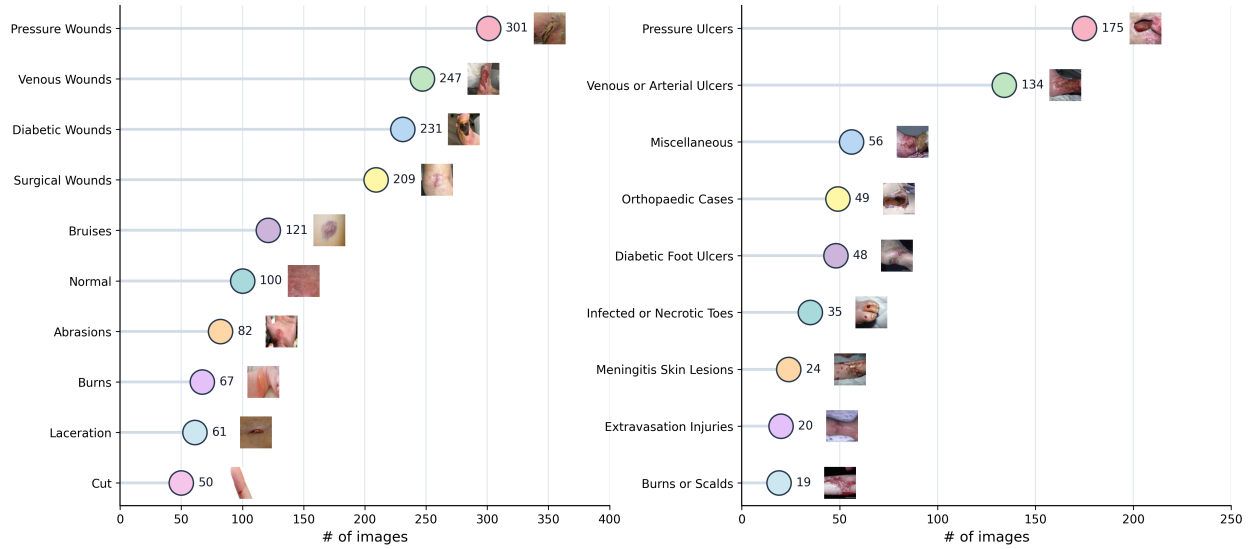

Figure 2: Class distributions for the Kaggle dataset (left) and the Medetec dataset (right). Images are taken from the corresponding datasets.

3.4 Support retrieval

For query-conditioned retrieval, the frozen OpenAI CLIP ViT-B/32 image encoder [59] was used to map each image to a 512-dimensional embedding vector. For each support image $I_j \in \mathcal{D}_{\text{sup}}$, an embedding was precomputed as

$$z_j = f_I(I_j),$$

and for each query image $I_q \in \mathcal{D}_{\text{eval}}$, an analogous embedding was computed as

$$z_q = f_I(I_q).$$

To place all representations on a common scale, each embedding was L2-normalised,

$$\hat{z}_i = \frac{z_i}{\|z_i\|_2},$$

so that angular proximity directly reflected semantic similarity in the shared feature space. Each candidate's support image was then scored using cosine similarity,

$$s(q, i) = \hat{z}_q^\top \hat{z}_i.$$

This shared embedding space, therefore, served as the basis for all query-conditioned support selection. Three strategies were considered for constructing the few-shot support context: random retrieval, k-nearest-neighbour (kNN) retrieval (or Retrieval-based In-Context Example Selection, RICES [4]), and kNN retrieval augmented with maximal marginal relevance (MMR) [16].

Random retrieval. Under random retrieval, support examples were sampled uniformly from $\mathcal{D}_{\text{sup}}$ without conditioning on the query image, with a unique random seed used for each request.

kNN retrieval. Given a query image I_q and a target context size K, kNN retrieval constructs the support context by selecting the K support images with the highest cosine-similarity scores $s(q, i)$.

kNN+MMR retrieval. To encourage diversity among relevant support examples, maximal marginal relevance was also used. In the kNN+MMR strategy, a candidate pool $\mathcal{C}_q$ of the top

M nearest neighbours of the query was retrieved according to $s(q, i)$, where $M > K$ and K denotes the final context size. From $\mathcal{C}_q$, the highest-similarity item was chosen. Each subsequent example, i_t, was selected from the remaining candidates in $\mathcal{C}_q$ as

$$i_t = \arg \max_{i \in \mathcal{C}_q \setminus \mathcal{R}_{t-1}} \left[\lambda s(q, i) - (1 - \lambda) \max_{j \in \mathcal{R}_{t-1}} \hat{z}_i^\top \hat{z}_j \right],$$

where $\lambda \in [0, 1]$ controls the trade-off between relevance and diversity. In the current study, λ was set to 0.7.

3.5 Models

We evaluated eleven multimodal language models from three families: Qwen 3.5 (0.8B, 2B, 4B, 9B, and 27B) [58], Ministral 3 (3B, 8B, and 14B) [50], and Gemma 4 (E2B, E4B, and 26B A4B) [29]. For consistency across experiments, all models were run with an 8192-token context window, thinking disabled, and temperature set to zero to make the outputs deterministic.

Experiments were run on a MacBook Pro with an Apple M4 Pro chip and 24 GB unified memory. The Qwen 3.5 checkpoints used `Q3_K_XL` quantisation. For Ministral 3, the 3B and 8B variants used `Q8_0`, whereas the 14B variant used `Q4_K_XL`. For Gemma 4, the E2B and E4B variants used `Q8_0`, whereas the 26B A4B variant used `UD-IQ3_S`. Because all evaluated systems were multimodal, each model was paired with a vision projector; Gemma 4 and Ministral 3 used BF16 projectors, whereas Qwen 3.5 used an F32 projector.

3.6 Prompts

All models were queried using a classification prompt so that differences in performance could be attributed primarily to model capacity and support-selection strategy rather than to prompt wording. In every condition, the query image was paired with a short instruction that asked the model to assign exactly one dataset label and return only that label string. For the Kaggle dataset class labels were: *Abrasions*, *Bruises*, *Burns*, *Cut*, *Diabetic Wounds*, *Laceration*, *Normal*, *Pressure Wounds*, *Surgical Wounds*, and *Venous Wounds*; for the Medetec dataset: *Burns or Scalds*, *Diabetic Foot Ulcers*, *Extravasation Injuries*, *Infected or Necrotic Toes*, *Meningitis Skin Lesions*, *Miscellaneous*, *Orthopaedic Cases*, *Pressure Ulcers*, and *Venous or Arterial Ulcers*.

In the zero-shot setting, the prompt consisted only of the task instruction and the query image, as illustrated in Figure 3. This setup measured each model's ability to classify wound images without any in-context visual references from the support set.

In the few-shot setting, the prompt began with a brief instruction informing the model that labelled example images would be shown before the final query. The prompt then included K retrieved support examples, each presented as an image–label pair in the form "*Example image for class y_i*", followed by the support image and its class label. After these support examples, the same

Zero-shot prompt

Query block: *Classify the wound shown in the query image.*
Choose exactly one label from: {class labels}.
Use the exact label spelling.
Reply with exactly one label name and nothing else.
Image: query image I_q

Figure 3: Zero-shot prompt structure.

query-classification block used in the zero-shot condition was appended, as shown in Figure 4. For random retrieval and standard kNN retrieval, K support examples were taken directly from the selected support set. For kNN+MMR retrieval, the final prompt still contained K examples, but these were reranked from an initial pool of M nearest neighbours before insertion into the prompt.

Few-shot prompt

Instruction block: *You will first see labelled example images for the dataset classes. Use them as visual references, then classify the final query image.*
Support examples: For each $i = 1, \ldots, K$, the prompt includes the text "*Example image for class* y_i", the corresponding support image I_i, and the class label y_i.
Query block: *Classify the wound shown in the query image.*
Choose exactly one label from: {class labels}.
Use the exact label spelling.
Reply with exactly one label name and nothing else.
Image: query image I_q

Figure 4: Few-shot (K-shot) prompt structure.

3.7 Retrieval influence diagnostics

To assess how closely retrieval-augmented SMLM predictions aligned with the retrieved embedding-space neighbourhood during ICL [49, 84], paired comparisons were conducted between each model and a retrieval-only control. The same diagnostics were applied to both kNN and kNN+MMR retrieval. For standard kNN, the global weighted-kNN baseline was used as the control. For kNN+MMR, the retrieval-only control was recomputed on the final reranked support set, so that the control reflected the exact diversity-filtered context shown to the model.

The weighted-kNN baseline was treated as a standard non-parametric classifier operating directly in the CLIP embedding space. For a query q, let $\mathcal{N}_K(q)$ denote the K labelled support images in $\mathcal{D}_{\text{sup}}$ with the largest cosine similarities to the query. The class score was the weighted sum of neighbour labels, and the predicted class was

$$\hat{y}_q^{\text{kNN}} = \arg\max_{c \in \mathcal{Y}} \sum_{i \in \mathcal{N}_K(q)} w(q,i)\mathbf{1}[y_i = c], \qquad w(q,i) = \frac{\max\{s(q,i), 0\}}{\sum_{j \in \mathcal{N}_K(q)} \max\{s(q,j), 0\}},$$

Here, c is a candidate class from the dataset-specific label set $\mathcal{Y}$, y_i is neighbour i's label, $\mathbf{1}[y_i = c]$ is the class-membership indicator, and $w(q,i)$ is the normalised non-negative cosine-similarity weight. For the matched kNN+MMR control, the same weighted-voting rule was applied to the final MMR-reranked neighbourhood shown in the prompt.

Statistical significance was assessed using accuracy, accuracy deltas, and a McNemar test, applied to correctness pairs to determine whether the SMLM significantly outperformed the baseline [47]. To further characterise behavioural alignment, raw prediction agreement and Cohen's κ were computed, with the latter adjusting for agreement expected by chance [21]. Prediction alignment with the retrieved support labels was quantified using three match-rate diagnostics: the top-1 match rate, the majority-label match rate, and the any-support match rate. To distinguish cases in which the SMLM succeeded on the same items as the retrieval-only control from those in which it added value beyond retrieval, a paired 2×2 correctness table was also analysed for each model–control comparison. From this table, two conditional correctness statistics were computed: $P(\text{SMLM correct} \mid \text{control correct})$, which quantifies how often the SMLM preserves retrieval-only

successes, and $P(\text{SMLM correct} \mid \text{control wrong})$, which quantifies how often the SMLM "rescues" retrieval-only failures. Fisher's exact test and the associated odds ratio were used to assess whether SMLM correctness was positively associated with control correctness beyond chance [27].

In these experiments, we used $K = 10$ support images for kNN retrieval and $K = 10$ with $M = 30$ for kNN+MMR retrieval.

3.8 Support set size impact

To assess how the size of the support set $\mathcal{D}_{\text{sup}}$ affects retrieval performance, we followed the procedure described by Xiong et al. [77]. In this procedure, the few-shot classification experiments are repeated for all retrieval methods using reduced support pools containing approximately 75% (914 for Kaggle, 353 for Medetec), 50% (610 for Kaggle, 235 for Medetec), and 25% (305 for Kaggle, 118 for Medetec) of the full support set. The full support set served as the benchmark. For each fraction, five subsets were sampled with different random seeds, while the evaluation set was kept fixed. To ensure fair comparisons, the same seed-specific subsets were used across all model and retrieval-method combinations within each fraction on both datasets. Performance on $\mathcal{D}_{\text{eval}}$ was then summarised as mean ± standard deviation over the five runs.

Two descriptive statistics were computed for each sampled support subset to help assess whether changes in accuracy were more plausibly attributable to class imbalance or to reduced embedding-space diversity. Let $\{(I_i, y_i)\}_{i=1}^{n} \subseteq \mathcal{D}_{\text{sup}}$ denote a sampled support subset of size n, and let $\mathcal{S} = \{(\hat{z}_i, y_i)\}_{i=1}^{n}$ be the corresponding set of embedding-label pairs, where $\hat{z}_i$ is the L2-normalized CLIP embedding of image I_i.

First, class-balance evenness was measured using the normalised Shannon entropy of the empirical class distribution, with larger values indicating a more even spread of support examples across C classes. If n_c is the number of support examples from class c and $p_c = n_c/n$, then

$$E_{\text{class}} = -\frac{1}{\log C} \sum_{c=1}^{C} p_c \log p_c.$$

Second, the geometric diversity of the subset was measured through the effective rank of its embedding covariance spectrum. Let

$$\Sigma_{\mathcal{S}} = \frac{1}{n} \sum_{i=1}^{n} (\hat{z}_i - \bar{z})(\hat{z}_i - \bar{z})^{\top}$$

be the covariance matrix of the subset embeddings, where $\bar{z} = \frac{1}{n} \sum_{i=1}^{n} \hat{z}_i$ is the sample mean. If $\{\sigma_m\}_{m=1}^{d}$ are the eigenvalues of $\Sigma_{\mathcal{S}}$, we normalize them as

$$\tilde{\sigma}_m = \frac{\sigma_m}{\sum_{r=1}^{d} \sigma_r},$$

and define the effective rank as

$$r_{\text{eff}} = \exp\left(- \sum_{m=1}^{d} \tilde{\sigma}_m \log \tilde{\sigma}_m \right).$$

A larger effective rank indicates that variance is distributed across more dimensions, suggesting broader representational coverage of the support pool. For each support fraction, both E_{class} and r_{eff} were computed across the five seeds as mean ± standard deviation.

To evaluate how data scarcity affects ICL in comparison with conventional supervised methods, we additionally trained deep learning image classifiers on the same support sets used for ICL and repeated the experiment on subsets of both datasets. Each support pool was split internally into an 80/20 train/validation subset, and final performance was measured on the corresponding $\mathcal{D}_{\text{eval}}$ sets. We evaluated four popular ImageNet-pretrained backbones: ViT-B/16 [24], ConvNeXt-Tiny [43], EfficientNetV2-S [68], and ResNet50 [32]. For each backbone, we compared full fine-tuning with a head-only transfer-learning setting in which the pretrained feature extractor was frozen and only the classification head was updated. For ViT-B/16, we additionally evaluated a LoRA variant ($r = 8$, $\alpha = 16$, dropout 0.05) in which the pretrained ViT weights were frozen and only lightweight LoRA adapters plus the classification head were trained [34]. All models were trained with AdamW optimiser, weight decay 10^{-4}, batch size of 16 for 30 epochs with early stopping. Learning rates ranged from 1×10^{-5} to 1×10^{-3} depending on backbone and tuning mode. Training images were resized to the model input size and augmented with random horizontal flips ($p = 0.5$), random rotations within $\pm 8°$, and colour jitter (brightness 0.12, contrast 0.12, saturation 0.08), followed by ImageNet normalisation; validation and test images were only resized and normalised.

3.9 Support context size impact

To measure how context size affects both classification performance and inference cost, we conducted a support-count sweep in which the number of support images shown to the SMLM during ICL was varied while the support pool, evaluation set, prompt template, and model settings were kept fixed. We evaluated context sizes from $K = 2$ to $K = 20$ in steps of two images. For each condition, we report accuracy, the mean model-reported input token count, and the average response time per processed request.

4 Results

4.1 In-context learning significantly improves classification performance

Table 1 shows the results on the Kaggle wound dataset. Notably, few-shot prompting with query-conditioned retrieval consistently improved performance over zero-shot prompting by a substantial margin, whereas random few-shot context provided only modest gains. This indicates that the benefits from ICL depend largely on the retrieval strategy of support examples. The strongest overall results were obtained by Gemma 4 26B A4B and the larger Qwen 3.5 models: Gemma 4 26B A4B reached 0.868 accuracy under kNN (95% CI [0.824, 0.908]), while Qwen 3.5 27B and 9B reached 0.872 and 0.868 under kNN+MMR (95% CIs [0.828, 0.912] and [0.824, 0.908], respectively). By contrast, zero-shot performance was much lower and more variable, ranging from 0.128 for Qwen 3.5 0.8B (95% CI [0.088, 0.172]) to 0.648 for Gemma 4 26B A4B (95% CI [0.588, 0.704]).

The effect of query-specific retrieval relative to zero-shot and random few-shot prompting was especially pronounced for several smaller and mid-sized models. For example, Qwen 3.5 2B improved from 0.280 (95% CI [0.228, 0.336]) in the zero-shot setting to 0.748 (95% CI [0.696, 0.796]) with kNN+MMR, and Qwen 3.5 4B improved from 0.316 (95% CI [0.260, 0.376]) to 0.788 (95% CI [0.732, 0.836]). Similar gains were also observed for Ministral 3 14B, which increased from 0.364 (95% CI [0.304, 0.424]) to 0.752 (95% CI [0.692, 0.804]) under kNN, and for Gemma 4 E4B, which rose from 0.400 (95% CI [0.336, 0.464]) to 0.736 (95% CI [0.680, 0.788]). Relative to the retrieval-only weighted-kNN baseline, which achieved 0.708 accuracy (95% CI [0.648, 0.764]), the strongest query-conditioned ICL configurations achieved clear gains, whereas all zero-shot settings and several smaller retrieval-augmented models remained below this benchmark.

Table 1: Performance comparison of zero-shot and few-shot classification across models on the Kaggle dataset, reported in terms of accuracy and F1. The best result for each model is highlighted in bold. For both kNN and kNN+MMR, the final few-shot context contained $K = 10$ support images; for kNN+MMR, these were selected from an initial candidate pool of $M = 30$ nearest neighbors. The table also includes a retrieval-only, embedding-based weighted-kNN baseline for comparison.

Model	**Zero-shot**		**Few-shot (Random)**		**Few-shot (kNN)**		**Few-shot (kNN+MMR)**	
	Acc.	**F1**	**Acc.**	**F1**	**Acc.**	**F1**	**Acc.**	**F1**
Qwen 3.5								
27B	0.580	0.536	0.636	0.624	0.860	0.862	**0.872**	**0.871**
9B	0.544	0.510	0.640	0.615	0.836	0.833	**0.868**	**0.865**
4B	0.316	0.241	0.456	0.422	0.780	0.780	**0.788**	**0.789**
2B	0.280	0.173	0.324	0.266	0.704	0.680	**0.748**	**0.726**
0.8B	0.128	0.078	0.196	0.155	**0.328**	**0.327**	0.300	0.293
Ministral 3								
14B	0.364	0.348	0.448	0.447	**0.752**	**0.758**	0.708	0.712
8B	0.308	0.296	0.440	0.424	**0.656**	0.650	**0.656**	**0.653**
3B	0.308	0.251	0.392	0.334	0.548	0.525	**0.580**	**0.558**
Gemma 4								
26B A4B	0.648	0.643	0.652	0.647	**0.868**	**0.868**	0.864	0.864
E4B	0.400	0.342	0.424	0.405	**0.736**	**0.732**	0.716	0.706
E2B	0.304	0.262	0.332	0.296	**0.456**	**0.434**	0.444	0.426
Weighted-kNN	0.708	0.701						

Table 2 shows the corresponding results on the Medetec dataset. The same broad pattern was observed, although absolute performance was lower than on the Kaggle dataset. The strongest overall result was obtained by Qwen 3.5 27B under kNN+MMR, reaching 0.678 accuracy. Other strong results were obtained by Qwen 3.5 4B, with 0.622 accuracy under kNN+MMR, Qwen 3.5 9B, with 0.611 accuracy under kNN+MMR, and Gemma 4 26B A4B, with 0.611 accuracy under kNN+MMR. By contrast, zero-shot performance was considerably lower, ranging from 0.089 for Qwen 3.5 0.8B (95% CI [0.033, 0.156]) to 0.400 for Gemma 4 26B A4B (95% CI [0.300, 0.500]). Random few-shot prompting produced only modest and inconsistent gains, and query-conditioned retrieval produced large gains across most models. Qwen 3.5 2B improved from chance-level 0.144 accuracy (95% CI [0.078, 0.222]) in the zero-shot setting to 0.567 (95% CI [0.467, 0.667]) with kNN+MMR, while Qwen 3.5 4B improved from 0.244 (95% CI [0.156, 0.344]) to 0.622 (95% CI [0.522, 0.722]). Similar improvements were observed for other model families: Ministral 3 14B increased from 0.244 accuracy (95% CI [0.156, 0.333]) to 0.500 (95% CI [0.400, 0.600]) under both kNN and kNN+MMR, and Gemma 4 E4B increased from 0.256 (95% CI [0.167, 0.344]) to 0.533 (95% CI [0.433, 0.644]) under kNN. As in the Kaggle dataset, the best retrieval-augmented multimodal configurations outperformed the retrieval-only weighted-kNN baseline, which reached 0.467 accuracy (95% CI [0.367, 0.567]).

Taken together, the Kaggle and Medetec results show a consistent hierarchy of prompting strategies. Zero-shot prompting was weakest, random few-shot prompting provided only limited and unreliable gains, and query-conditioned retrieval produced the largest improvements. Across model families, standard kNN was generally a strong and consistent retrieval strategy, whereas kNN+MMR usually provided only modest additional gains, primarily within the Qwen family.

Table 2: Performance comparison of zero-shot and few-shot classification across models on the Medetec dataset, reported in terms of accuracy and F1. The best result for each model is highlighted in bold. For both kNN and kNN+MMR, the final few-shot context contained $K = 10$ support images; for kNN+MMR, these were selected from an initial candidate pool of $M = 30$ nearest neighbors. The table also includes a retrieval-only, embedding-based weighted-kNN baseline for comparison.

Model	Zero-shot		Few-shot (Random)		Few-shot (kNN)		Few-shot (kNN+MMR)	
	Acc.	F1	Acc.	F1	Acc.	F1	Acc.	F1
Qwen 3.5								
27B	0.367	0.321	0.389	0.342	0.633	0.629	**0.678**	**0.670**
9B	0.333	0.303	0.278	0.251	0.600	0.589	**0.611**	**0.614**
4B	0.244	0.142	0.333	0.320	0.578	0.562	**0.622**	**0.601**
2B	0.144	0.104	0.222	0.196	0.533	0.528	**0.567**	**0.573**
0.8B	0.089	0.031	0.167	0.112	**0.244**	**0.220**	0.200	0.176
Ministral 3								
14B	0.244	0.158	0.356	0.286	**0.500**	**0.480**	**0.500**	0.477
8B	0.244	0.163	0.344	0.306	0.444	0.403	**0.456**	**0.427**
3B	0.200	0.129	0.189	0.165	0.322	0.293	**0.389**	**0.387**
Gemma 4								
26B A4B	0.400	0.378	0.422	0.428	0.567	0.561	**0.611**	**0.606**
E4B	0.256	0.217	0.300	0.244	**0.533**	**0.508**	0.511	0.489
E2B	0.156	0.128	0.133	0.119	**0.367**	**0.324**	0.289	0.272
Weighted-kNN	0.467	0.447						

The Kaggle dataset yielded higher absolute performance, with top accuracy above 0.87, whereas the best Medetec result reached 0.678 accuracy. Nevertheless, the main trend was stable across both datasets: retrieval-based ICL accounted for most of the performance lift, while the stronger multimodal SMLMs surpassed the retrieval-only baseline by a clear margin.

4.2 Larger models are more likely to improve beyond retrieval-only baselines

For the Kaggle dataset, Table 3 summarises the primary paired comparison against the retrieval-only control for kNN ICL: Qwen 3.5 27B, Qwen 3.5 9B, and Gemma 4 26B A4B exceeded the weighted-kNN baseline (0.708 accuracy) by +0.152, +0.128, and +0.160, respectively, with exact McNemar tests indicating significant paired improvements. At the same time, their support-overlap rates remained high: top-1 support matches ranged from 0.708 to 0.732, support-majority matches from 0.720 to 0.744, and any-support matches from 0.952 to 0.980. Conditional correctness analysis showed the same pattern: for these three models, the probability of being correct when the weighted-kNN control was correct remained very high (0.938–0.966), while the probability of being correct when the weighted-kNN control was wrong was still substantial (0.589–0.630), with Fisher exact tests indicating strong positive association between SMLM and control correctness (odds ratios = 10.53–16.73, all $p < 10^{-9}$; see Appendix A). This pattern indicates that their predictions were strongly constrained by the retrieved support, yet were not reducible to a simple nearest-neighbour vote, because agreement and κ remained substantial rather than near-perfect, and the models still achieved significant gains over the weighted-kNN control. Qwen 3.5 4B also remained above the weighted-kNN control (+0.072; McNemar $p = 0.011$), but by a smaller margin; correspondingly, it

Table 3: Paired retrieval-control comparisons for kNN few-shot prompting against the global weighted-kNN control (accuracy = 0.708) on the Kaggle dataset. Top-1, Maj., and Any denote match rates to the top retrieved support label, the support-majority label, and any label present in the retrieved support set, respectively. Ret. denotes P(SMLM correct | control correct), and Resc. denotes P(SMLM correct | control wrong). Agreement denotes the raw prediction agreement rate with the control, and κ denotes Cohen's kappa.

Model	**Acc.**	Δ	**McNemar** p	**Top-1**	**Maj.**	**Any**	**Ret.**	**Resc.**	**Agreement**	κ
Qwen 3.5 27B	0.860	+0.152	< 0.001	0.732	0.744	0.980	0.960	0.616	0.752	0.723
Qwen 3.5 9B	0.836	+0.128	< 0.001	0.716	0.740	0.964	0.938	0.589	0.740	0.710
Gemma 4 26B A4B	0.868	+0.160	< 0.001	0.708	0.720	0.952	0.966	0.630	0.728	0.697
Qwen 3.5 4B	0.780	+0.072	0.011	0.704	0.752	0.984	0.921	0.438	0.744	0.713
Ministral 3 14B	0.752	+0.044	0.169	0.684	0.680	0.944	0.881	0.438	0.692	0.656
Gemma 4 E4B	0.736	+0.028	0.401	0.720	0.716	0.948	0.876	0.397	0.712	0.676
Qwen 3.5 2B	0.704	-0.004	1.000	0.676	0.716	0.928	0.853	0.342	0.720	0.687
Ministral 3 8B	0.656	-0.052	0.130	0.640	0.632	0.884	0.785	0.342	0.640	0.595
Ministral 3 3B	0.548	-0.160	< 0.001	0.528	0.508	0.768	0.633	0.342	0.504	0.449
Gemma 4 E2B	0.456	-0.252	< 0.001	0.436	0.432	0.668	0.520	0.301	0.424	0.358
Qwen 3.5 0.8B	0.328	-0.380	< 0.001	0.296	0.292	0.608	0.362	0.247	0.296	0.207

preserved most weighted-kNN-correct cases (0.921) but rescued a more modest fraction of weighted-kNN errors (0.438).

By contrast, the weaker models showed lower agreement with the weighted-kNN control and weaker support overlap. Qwen 3.5 2B was already at parity with the control ($\Delta = -0.004$), although still demonstrating strong conditional dependence on the weighted-kNN baseline (retention 0.853, rescue 0.342; Fisher $p < 10^{-14}$), the cases it rescued were nearly offset by cases in which the control had been correct, and the SMLM was not. Smaller models such as Gemma 4 E2B, Ministral 3 3B, and Qwen 3.5 0.8B had substantially lower agreement values (0.424, 0.504, and 0.296, respectively) and κ values (0.358, 0.449, and 0.207), with lower any-support overlap (0.668, 0.768, and 0.608). Together with their lower conditional retention and rescue rates, this suggests that the smaller models were less consistently anchored to the retrieved neighbourhood and made less effective use of ICL.

For the Medetec dataset, Table 4 summarises the analogous paired retrieval-control comparisons for the kNN retrieval. The global weighted-kNN control reached 0.467 accuracy, and Qwen 3.5 27B and 9B exceeded it by +0.167 and +0.133, with an exact McNemar test indicating a significant paired improvement. By contrast, Gemma 4 26B A4B and Qwen 3.5 4B achieved positive deltas of +0.100 and +0.111, respectively, but these differences were not significant. The strongest models remained closely tied to the retrieved support: Qwen 3.5 27B had a support-majority match rate of 0.744 and an any-support match rate of 0.978, while Qwen 3.5 9B had an any-support match rate of 1.000. Conditional correctness analysis showed that these models preserved most control-correct cases, with retention rates of 0.952 and 0.857, while rescuing a smaller fraction of control errors, with rescue rates of 0.354 and 0.375. Fisher's exact tests indicated a strong positive association between SMLM and control correctness for both models (odds ratios = 36.47 and 10.00; see Appendix A).

Several models showed a different pattern on Medetec: they were strongly coupled to the retrieval-only control but did not rescue enough control errors to obtain a significant net improvement. Gemma 4 E4B, for example, had high retention (0.905) and a strong association with the control (odds ratio = 36.10), but its rescue rate was only 0.208, and its accuracy gain over the control was not significant. Similarly, Qwen 3.5 2B had a positive but non-significant delta of +0.067. At the lower end, Ministral 3 3B and Qwen 3.5 0.8B fell significantly below the retrieval-only control. Qwen 3.5 0.8B was particularly weakly anchored to the retrieved neighbourhood, with low

Table 4: Paired retrieval-control comparisons for kNN few-shot prompting against the global weighted-kNN control (accuracy = 0.467) on the Medetec dataset. Top-1, Maj., and Any denote match rates to the top retrieved support label, the support-majority label, and any label present in the retrieved support set, respectively. Ret. denotes P(SMLM correct | control correct), and Resc. denotes P(SMLM correct | control wrong). Agreement denotes the raw prediction agreement rate with the control, and κ denotes Cohen's kappa.

Model	**Acc.**	**Δ**	**McNemar p**	**Top-1**	**Maj.**	**Any**	**Ret.**	**Resc.**	**Agreement**	**κ**
Qwen 3.5 27B	0.633	+0.167	< 0.001	0.611	0.744	0.978	0.952	0.354	0.733	0.660
Qwen 3.5 9B	0.600	+0.133	0.023	0.522	0.589	1.000	0.857	0.375	0.578	0.498
Gemma 4 26B A4B	0.567	+0.100	0.108	0.522	0.544	0.911	0.810	0.354	0.533	0.446
Qwen 3.5 4B	0.578	+0.111	0.076	0.433	0.567	0.844	0.810	0.375	0.556	0.483
Ministral 3 14B	0.500	+0.033	0.701	0.533	0.544	0.933	0.714	0.312	0.533	0.441
Gemma 4 E4B	0.533	+0.067	0.180	0.600	0.700	0.978	0.905	0.208	0.689	0.608
Qwen 3.5 2B	0.533	+0.067	0.362	0.444	0.444	0.922	0.714	0.375	0.433	0.364
Ministral 3 8B	0.444	-0.022	0.839	0.500	0.511	0.811	0.690	0.229	0.511	0.411
Gemma 4 E2B	0.367	-0.100	0.150	0.422	0.289	0.744	0.524	0.229	0.289	0.216
Ministral 3 3B	0.322	-0.144	0.029	0.289	0.322	0.767	0.476	0.188	0.311	0.240
Qwen 3.5 0.8B	0.244	-0.222	0.005	0.156	0.100	0.467	0.214	0.271	0.100	0.041

support-overlap values, very low agreement with the control, and no significant association between SMLM and control correctness.

Because the kNN+MMR retrieval changed only the final support-set selection step, its retrieval-control diagnostics are not repeated in full here. Across both datasets, the kNN+MMR results followed the same qualitative pattern as standard kNN: larger models retained most retrieval-control successes while rescuing a subset of retrieval-control failures, whereas smaller models showed weaker evidence of reasoning beyond the retrieved neighbourhood. Detailed kNN+MMR paired results are reported in Appendix B.

Overall, the results show that larger models make more effective use of ICL without merely "parroting" the support context. Conditional correctness analysis makes the size distinction clearer: the larger models preserve most cases that the retrieval-only control gets right while also "rescuing" a subset of the control's errors. In other words, they remain guided by the retrieved neighbourhood while still outperforming retrieval-only controls on the same examples, and their agreement with those controls is substantial but far from perfect. The smaller models also benefit from relevant retrieved examples compared with zero-shot and random few-shot prompting, but they either use ICL without achieving any improvement or fail to exploit it reliably, consistently falling below what retrieval alone achieves on the same context.

4.3 ICL performance with SMLMs degrades modestly under reduced support

Table 5 shows that the reduced support subsets remained broadly class-balanced across fractions. For Kaggle, class-balance evenness changed only slightly, from 0.889 for the full support set to 0.879 at the 25% fraction. Medetec showed a similarly small mean change, from 0.808 to 0.799, although variability increased at the smallest support size. By contrast, the effective rank of the CLIP embedding space decreased more clearly as support size was reduced, from 52.9 to 45.5 for Kaggle and from 56.0 to 38.3 for Medetec. This suggests that the support-size ablation primarily reduced embedding-space coverage rather than causing large class-balance shifts, particularly for Medetec where the smaller support pool lost representational diversity more quickly.

Table 6 reports the accuracy trends across support fractions on the Kaggle dataset. The strongest retrieval-based SMLMs degraded only moderately as the support pool was reduced. Qwen 3.5 27B with kNN+MMR changed from 0.872 at full support to 0.830 at the 50% fraction

Table 5: Support-set size and subset statistics across the support-set-size ablation for different subset selection seeds: subset size (n), class-balance evenness (E_{class}), and effective rank (r_{eff}).

Dataset	**Metric**	**100%**	**75%**	**50%**	**25%**
Kaggle	n	1219	914	610	305
	E_{class}	0.889	0.889 ± 0.002	0.888 ± 0.006	0.879 ± 0.005
	r_{eff}	52.9	51.7 ± 0.1	49.3 ± 0.6	45.5 ± 1.2
Medetec	n	470	353	235	118
	E_{class}	0.808	0.809 ± 0.009	0.804 ± 0.012	0.799 ± 0.048
	r_{eff}	56.0	53.2 ± 0.5	48.1 ± 0.4	38.3 ± 0.8

(−4.8%) and 0.781 at the 25% fraction (−10.4%). Gemma 4 26B A4B was also robust, reaching 0.829 at the 50% fraction (−4.5%) and 0.794 at the 25% fraction (−8.5%) with kNN+MMR, and 0.848 at the 50% fraction (−1.9%) and 0.798 at the 25% fraction (−7.6%) with standard kNN. Qwen 3.5 27B with standard kNN and Qwen 3.5 9B with kNN+MMR showed similar reductions at the 25% fraction, reaching 0.769 (−10.6%) and 0.763 (−12.1%), respectively. The supervised baselines lost more performance at the smallest training size: the best supervised result at 25% was 0.666 for ConvNeXt-Tiny with full fine-tuning, down from 0.804 at full support (−17.2%).

The lower-capacity and random-context conditions showed a different pattern. Random few-shot prompting remained substantially below query-conditioned retrieval throughout the sweep, and its accuracy changed only weakly with support-pool size, suggesting that the main advantage came from retrieving relevant examples rather than from simply having a larger pool of support images. Smaller retrieval-augmented models also benefited from kNN or kNN+MMR selection, but their absolute performance was lower, and their trends were less monotonic. This is consistent with the earlier retrieval-control results: retrieved context remained useful, but the strongest gains under support reduction were concentrated in the larger SMLMs.

Table 7 shows the same support-fraction analysis for the Medetec dataset. Absolute accuracies were lower than on Kaggle, and the reduction from full support was larger for several methods. Qwen 3.5 27B with kNN+MMR decreased from 0.678 to 0.527 at the 25% fraction (−22.3%), while the kNN version decreased from 0.633 to 0.518 (−18.2%). Gemma 4 26B A4B with kNN+MMR was more stable, decreasing from 0.611 to 0.529 (−13.4%). These retrieval-based SMLM results still exceeded the supervised baselines at the smallest training size. At the 25% fraction, the best SMLM results were around 0.52–0.53 accuracy, whereas the best supervised result was 0.413 for ConvNeXt-Tiny with head fine-tuning, down from 0.644 at full support (−35.9%).

The stronger degradation on Medetec is consistent with the subset statistics in Table 5. The effective rank decreased from 56.0 to 38.3 on Medetec (−31.6%), compared with 52.9 to 45.5 on Kaggle (−14.0%). Thus, the smaller Medetec support pool lost embedding-space coverage more quickly. Nevertheless, the strongest retrieval-based SMLM conditions retained a clear advantage over both random prompting and supervised training at the smallest fractions. Overall, Tables 6 and 7 indicate that retrieval-based ICL is fairly robust to moderate support reduction, but that performance starts to decline when the support pool becomes too small or too narrow.

Table 6: Accuracy across support fractions on the Kaggle dataset. The 1.0 column contains single-run values; the other columns show mean ± std across five seeds. Rows are grouped into supervised image models and non-supervised retrieval-based methods. For supervised models, *full* denotes full fine-tuning with an unfrozen backbone, *LoRA* denotes training lightweight low-rank adapters, and *head* denotes training only the final classification layer with the backbone frozen.

Model	1.0	0.75	0.50	0.25
Supervised models				
ViT-B/16 full	0.808	0.766 ± 0.027	0.706 ± 0.023	0.642 ± 0.019
ConvNeXt-Tiny full	0.804	0.779 ± 0.022	0.765 ± 0.025	0.666 ± 0.028
ViT-B/16 LoRA r=8	0.788	0.778 ± 0.025	0.733 ± 0.023	0.648 ± 0.037
EfficientNet V2-S full	0.772	0.786 ± 0.014	0.716 ± 0.024	0.626 ± 0.061
ResNet50 full	0.760	0.734 ± 0.028	0.685 ± 0.013	0.626 ± 0.044
ViT-B/16 head	0.716	0.718 ± 0.036	0.683 ± 0.030	0.639 ± 0.026
ConvNeXt-Tiny head	0.700	0.730 ± 0.025	0.698 ± 0.010	0.643 ± 0.027
ResNet50 head	0.676	0.656 ± 0.041	0.603 ± 0.031	0.560 ± 0.022
EfficientNet V2-S head	0.644	0.562 ± 0.024	0.519 ± 0.026	0.482 ± 0.015
SMLMs				
Qwen 3.5 27B kNN+MMR	0.872	0.873 ± 0.011	0.830 ± 0.040	0.781 ± 0.025
Gemma 4 26B A4B kNN+MMR	0.868	0.852 ± 0.016	0.829 ± 0.019	0.794 ± 0.019
Qwen 3.5 9B kNN+MMR	0.868	0.849 ± 0.010	0.823 ± 0.017	0.763 ± 0.010
Gemma 4 26B A4B kNN	0.864	0.845 ± 0.006	0.848 ± 0.025	0.798 ± 0.022
Qwen 3.5 27B kNN	0.860	0.851 ± 0.013	0.829 ± 0.012	0.769 ± 0.013
Qwen 3.5 9B kNN	0.836	0.825 ± 0.017	0.816 ± 0.019	0.743 ± 0.022
Ministral 3 14B kNN	0.752	0.694 ± 0.016	0.671 ± 0.010	0.628 ± 0.026
Qwen 3.5 2B kNN+MMR	0.748	0.719 ± 0.018	0.705 ± 0.013	0.646 ± 0.020
Gemma 4 E4B kNN	0.736	0.706 ± 0.011	0.680 ± 0.014	0.623 ± 0.007
Gemma 4 E4B kNN+MMR	0.716	0.692 ± 0.012	0.696 ± 0.006	0.647 ± 0.017
Ministral 3 14B kNN+MMR	0.708	0.710 ± 0.020	0.674 ± 0.029	0.633 ± 0.016
Qwen 3.5 2B kNN	0.704	0.713 ± 0.009	0.694 ± 0.025	0.637 ± 0.018
Ministral 3 8B kNN+MMR	0.656	0.639 ± 0.008	0.611 ± 0.016	0.573 ± 0.013
Ministral 3 8B kNN	0.656	0.630 ± 0.017	0.602 ± 0.026	0.573 ± 0.026
Gemma 4 26B A4B Random	0.652	0.640 ± 0.016	0.644 ± 0.005	0.642 ± 0.023
Qwen 3.5 9B Random	0.640	0.619 ± 0.020	0.616 ± 0.014	0.624 ± 0.017
Qwen 3.5 27B Random	0.636	0.623 ± 0.009	0.609 ± 0.014	0.607 ± 0.025
Ministral 3 3B kNN+MMR	0.580	0.563 ± 0.017	0.553 ± 0.023	0.506 ± 0.029
Ministral 3 3B kNN	0.548	0.534 ± 0.016	0.529 ± 0.026	0.496 ± 0.019
Gemma 4 E2B kNN	0.456	0.494 ± 0.012	0.508 ± 0.020	0.476 ± 0.007
Ministral 3 14B Random	0.448	0.449 ± 0.014	0.459 ± 0.027	0.457 ± 0.030
Gemma 4 E2B kNN+MMR	0.444	0.469 ± 0.013	0.483 ± 0.010	0.461 ± 0.014
Gemma 4 E4B Random	0.424	0.452 ± 0.006	0.444 ± 0.008	0.445 ± 0.007
Ministral 3 3B Random	0.392	0.400 ± 0.013	0.410 ± 0.011	0.419 ± 0.013
Ministral 3 8B Random	0.440	0.383 ± 0.013	0.403 ± 0.023	0.417 ± 0.028
Gemma 4 E2B Random	0.332	0.309 ± 0.027	0.339 ± 0.024	0.331 ± 0.017
Qwen 3.5 2B Random	0.324	0.351 ± 0.014	0.356 ± 0.013	0.341 ± 0.018

4.4 Increasing support-context size gives positive but diminishing returns

Figure 5 summarises the sweep over support-context sizes from 2 to 20 images. Accuracy generally increased with increasing context size, with the clearest gains in the lower part of the sweep (2-10

Table 7: Accuracy across support fractions on the Medetec dataset. The 1.0 column contains single-run values; the other columns show mean ± std across five seeds. Rows are grouped into supervised image models and non-supervised retrieval-based methods. For supervised models, *full* denotes full fine-tuning with an unfrozen backbone, *LoRA* denotes training lightweight low-rank adapters, and *head* denotes training only the final classification layer with the backbone frozen.

Model	1.0	0.75	0.50	0.25
Supervised image models				
ConvNeXt-Tiny head	0.644	0.578 ± 0.008	0.522 ± 0.055	0.413 ± 0.096
ConvNeXt-Tiny full	0.567	0.551 ± 0.033	0.491 ± 0.053	0.384 ± 0.061
ViT-B/16 head	0.567	0.511 ± 0.054	0.471 ± 0.068	0.398 ± 0.085
ViT-B/16 LoRA r=8	0.556	0.511 ± 0.053	0.480 ± 0.064	0.389 ± 0.067
EfficientNet V2-S full	0.556	0.487 ± 0.055	0.467 ± 0.072	0.327 ± 0.081
ResNet50 head	0.556	0.507 ± 0.026	0.442 ± 0.043	0.287 ± 0.100
ViT-B/16 full	0.533	0.529 ± 0.006	0.462 ± 0.069	0.376 ± 0.062
ResNet50 full	0.522	0.489 ± 0.050	0.427 ± 0.052	0.353 ± 0.084
EfficientNet V2-S head	0.433	0.422 ± 0.021	0.396 ± 0.051	0.293 ± 0.045
SMLMs				
Qwen 3.5 27B kNN+MMR	0.678	0.633 ± 0.023	0.577 ± 0.022	0.527 ± 0.074
Qwen 3.5 27B kNN	0.633	0.611 ± 0.021	0.555 ± 0.013	0.518 ± 0.076
Gemma 4 26B A4B kNN+MMR	0.611	0.604 ± 0.006	0.582 ± 0.056	0.529 ± 0.077
Qwen 3.5 9B kNN+MMR	0.611	0.562 ± 0.036	0.531 ± 0.021	0.458 ± 0.068
Qwen 3.5 9B kNN	0.600	0.578 ± 0.021	0.513 ± 0.034	0.467 ± 0.053
Gemma 4 26B A4B kNN	0.567	0.569 ± 0.018	0.540 ± 0.027	0.522 ± 0.060
Qwen 3.5 2B kNN+MMR	0.567	0.529 ± 0.023	0.467 ± 0.057	0.404 ± 0.076
Gemma 4 E4B kNN	0.533	0.524 ± 0.033	0.449 ± 0.034	0.427 ± 0.059
Qwen 3.5 2B kNN	0.533	0.513 ± 0.009	0.433 ± 0.050	0.382 ± 0.048
Gemma 4 E4B kNN+MMR	0.511	0.493 ± 0.029	0.469 ± 0.043	0.431 ± 0.033
Ministral 3 14B kNN+MMR	0.500	0.482 ± 0.025	0.440 ± 0.006	0.422 ± 0.048
Ministral 3 14B kNN	0.500	0.449 ± 0.025	0.443 ± 0.008	0.409 ± 0.043
Ministral 3 8B kNN+MMR	0.456	0.436 ± 0.024	0.407 ± 0.023	0.389 ± 0.038
Ministral 3 8B kNN	0.444	0.442 ± 0.016	0.424 ± 0.042	0.389 ± 0.046
Gemma 4 26B A4B Random	0.422	0.415 ± 0.050	0.427 ± 0.033	0.416 ± 0.042
Ministral 3 3B kNN+MMR	0.389	0.327 ± 0.017	0.353 ± 0.041	0.309 ± 0.032
Qwen 3.5 27B Random	0.388	0.402 ± 0.015	0.406 ± 0.020	0.424 ± 0.033
Gemma 4 E2B kNN	0.367	0.296 ± 0.030	0.264 ± 0.061	0.222 ± 0.028
Ministral 3 14B Random	0.356	0.329 ± 0.025	0.348 ± 0.024	0.338 ± 0.037
Ministral 3 8B Random	0.344	0.327 ± 0.043	0.358 ± 0.016	0.347 ± 0.048
Ministral 3 3B kNN	0.322	0.333 ± 0.022	0.344 ± 0.042	0.293 ± 0.030
Gemma 4 E2B Random	0.300	0.291 ± 0.021	0.329 ± 0.062	0.324 ± 0.016
Gemma 4 E2B kNN+MMR	0.289	0.271 ± 0.048	0.264 ± 0.033	0.216 ± 0.023
Qwen 3.5 9B Random	0.278	0.338 ± 0.032	0.362 ± 0.033	0.342 ± 0.029
Qwen 3.5 2B Random	0.222	0.242 ± 0.035	0.231 ± 0.039	0.233 ± 0.030
Ministral 3 3B Random	0.189	0.271 ± 0.047	0.296 ± 0.040	0.300 ± 0.014
Gemma 4 E4B Random	0.133	0.144 ± 0.029	0.147 ± 0.023	0.111 ± 0.014

images). Beyond this range, performance typically flattened or fluctuated, and the largest contexts did not yield consistent additional gains: from 2 to 10 support images, mean accuracy increased by 0.012 per two-image step for kNN and by 0.009 per two-image step for kNN+MMR. From 10 to 20 support images, the corresponding gains were only 0.001 and 0.002 per step, indicating that

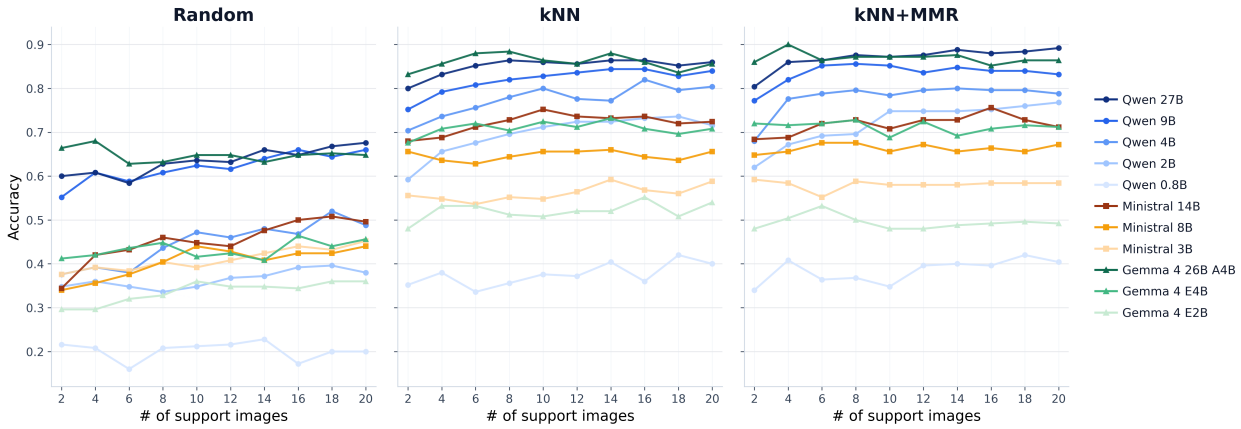

Figure 5: SMLM accuracy as a function of support-context size for different support-selection strategies.

larger contexts produced limited additional improvement.

Across the full sweep, retrieval-based context construction remained substantially stronger than random support sampling. Both kNN and kNN+MMR were consistently above the corresponding random-context results, while the difference between kNN and kNN+MMR was comparatively smaller, ranging from -0.004 to 0.020 accuracy points. The larger and mid-sized models showed clearer improvements as retrieved context was added, whereas the smallest models exhibited flatter and more variable trends.

The computational measures increased with context size. Mean response time rose with the number of support images for every model (see Table 8) and mean input-token counts also increased approximately linearly with context size within each model family, from 702 to 3958 tokens for Qwen 3.5, from 843 to 4652 for Ministral 3, and from 937 to 6042 for Gemma 4 (see Table 9).

Table 8: Mean response time in seconds per request by model and number of support images. Values are averaged across the three retrieval strategies.

Model	2	4	6	8	10	12	14	16	18	20
Qwen 3.5 27B	8.36	12.55	16.49	21.07	24.68	28.37	32.27	36.17	40.38	44.49
Qwen 3.5 9B	3.00	4.94	6.92	8.68	10.56	12.23	13.73	14.10	15.91	18.17
Qwen 3.5 4B	2.06	3.21	4.33	5.60	5.53	5.96	7.21	8.55	9.57	10.41
Qwen 3.5 2B	0.88	1.43	1.93	2.51	2.99	3.44	3.86	4.30	4.83	5.28
Qwen 3.5 0.8B	0.41	0.65	0.86	1.14	1.40	1.64	1.85	2.11	2.34	2.49
Ministral 3 14B	4.35	6.78	9.11	11.71	14.68	17.57	20.04	21.97	24.84	26.95
Ministral 3 8B	2.92	4.62	6.27	8.16	9.54	11.11	12.87	14.57	16.09	18.40
Ministral 3 3B	1.53	2.46	3.32	4.24	5.21	6.13	7.09	8.00	9.02	10.13
Gemma 4 26B A4B	3.98	6.59	9.36	12.30	14.79	18.96	20.52	22.89	25.38	28.89
Gemma 4 E4B	2.21	3.61	5.02	6.33	7.60	8.93	10.32	11.73	13.24	14.67
Gemma 4 E2B	1.48	2.48	3.43	4.36	5.37	6.58	7.91	8.59	9.60	10.60

Table 9: Mean input tokens per request by model family and number of support images.

Model family	2	4	6	8	10	12	14	16	18	20
Qwen 3.5	702	1099	1458	1853	2226	2560	2913	3262	3626	3958
Ministral 3	843	1305	1736	2173	2614	3020	3443	3851	4260	4652
Gemma 4	937	1503	2070	2637	3203	3772	4339	4907	5474	6042

5 Discussion

This study demonstrates that retrieval-augmented in-context learning (ICL) improves the capabilities of small multimodal language models, making them a viable and flexible approach for wound image classification, particularly under limited labelled data. Across both tested datasets, zero-shot and random few-shot prompting were consistently weaker than query-conditioned prompting, indicating that the choice of support examples is central to effective ICL. The strongest gains came from CLIP-based kNN retrieval and kNN+MMR retrieval, especially for the larger Qwen and Gemma models, which both benefited from relevant examples and outperformed matched retrieval-only weighted kNN controls. This suggests that the best-performing SMLMs successfully used retrieved context within the input prompt and merged it with internal knowledge gained during pretraining. At the same time, the experiments revealed practical limits: performance depended on model scale, retrieval strategy, dataset difficulty, and support-set coverage, while increasing the number of support images beyond a moderate context size yielded diminishing accuracy gains but higher latency and longer input lengths.

Tables 1 and 2 demonstrate that neither retrieval strategy is optimal across model families. For the Qwen family, the kNN+MMR retrieval strategy yielded the best performance, whereas for the Gemma family, kNN was the best strategy, with no clear winner for the Ministral model family. This indicates that, for a given problem and model, different retrieval strategies should be evaluated to identify the optimal solution. Notably, larger Qwen models (9B and 27B), as well as Gemma 4 26B A4B, achieved statistically significant improvements over the baseline weighted kNN classifier, as indicated by McNemar tests, while having very high retention scores. On the Kaggle dataset, those models retained 93–97% of the correct kNN predictions, whereas on the Medetec dataset, they retained at least 80% of the correct kNN predictions. These results indicate that the models were highly capable of identifying when the kNN prediction is correct, without being too dependent on the retrieved context, as indicated by agreement scores (see Tables 3 and 4). Particularly remarkable is the performance of Qwen 3.5 27B, which achieved a retention score of 0.952 even on the more challenging Medetec dataset. In addition to retention, the best-performing models exhibited substantial rescue scores: approximately 0.65 on Kaggle and 0.36 on Medetec. These values suggest that the models could filter out incorrect kNN predictions and select the correct alternative based on their internal knowledge. The statistical significance of these improvements further supports the conclusion that the models contribute meaningful corrective behaviour rather than random variation. Another important pattern is the high agreement with at least one label present in the support set. This further indicates that the models' corrective suggestions were strongly shaped by the contextual information provided in the support examples. While such context-dependence may introduce a form of support-set bias, potentially limiting performance when the support set is suboptimal, it may be advantageous when the support set is constructed through a targeted retrieval strategy rather than random sampling.

Tables 6 and 7 show that several larger retrieval-augmented SMLMs were comparable or even surpassed the classic supervised fine-tuned image classification models. This advantage was most evident with reduced support: with only 50% or 25% of the available support/training data, the best ICL-based SMLMs outperformed the best supervised baselines on both datasets. These results should not be interpreted as showing that ICL removes the need for labelled data: as with supervised learning, retrieval-based ICL still requires representative labelled examples, and Table 5 suggests that performance decreased as embedding-space coverage declined. The practical distinction is that ICL uses these examples at inference time rather than through parameter updates. As a result, the support pool or label set can be modified without retraining a classifier, making the approach more flexible when data distributions, clinical definitions, or deployment requirements

change. These results, therefore, suggest that retrieval-augmented ICL is not data-free, but it may be less data-hungry than conventional supervised training and able to remain useful with smaller labelled datasets.

The results from the support-context sweep experiment, shown in Figure 5 and Tables 8 and 9, highlighted a trade-off between accuracy and cost when using ICL with SMLMs. Adding more support images improved performance primarily up to a moderate context size (8-10 images); beyond that, the gains were small, while input length and response time continued to increase. In practice, this favours compact retrieved contexts rather than simply larger prompts: a small set of relevant examples appears to capture most of the ICL benefit with lower latency and computational cost. The gap between retrieved and random contexts again shows that relevance matters more than context size alone: additional examples help only when they provide useful evidence for the query image.

The performance differed between the Kaggle and Medetec datasets, although the overall trends were similar. The Medetec dataset was generally harder than the Kaggle one, potentially because its support set was approximately 2.5 times smaller. However, the support-set reduction experiments show that the best SMLMs on reduced Kaggle support sets (610 and 305 images) still outperformed their counterparts on the full Medetec support set (470 images). This suggests that differences in class definitions, visual heterogeneity, or inter-class separability may also have contributed to the lower Medetec performance.

A key limitation of these datasets for image-based classification is that some clinically distinct etiologies are grouped into a single class, reducing label specificity and increasing visual heterogeneity. For example, in the Medetec dataset, venous and arterial ulcers are merged into one category ("Venous or Arterial Ulcers"), despite having different underlying causes and characteristic appearances, which can include differences in wound shape, depth, exudate, and surrounding tissue condition [48]. This aggregation leads to high intra-class variability, making it harder for models to learn consistent visual patterns. Conversely, other classes across both datasets may exhibit overlapping visual features despite representing different conditions, further increasing inter-class ambiguity, a known challenge in medical image classification where distinctions between categories can be subtle even for experts [38, 75]. Additionally, the presence of broad or weakly defined categories (e.g., "Miscellaneous") and potential label noise due to subjective clinical annotation can further degrade model performance and generalisation. Future work should therefore evaluate SMLMs on additional wound datasets with broader wound-type coverage, as well as on medical image-classification tasks beyond wound analysis.

During experiments, refusal rates remained low overall (0.08% across all model outputs), despite some images containing potentially sensitive visual content. A plausible explanation is that all evaluated models were instruction-tuned: prior work shows that instruction tuning improves alignment with user intent and instruction-following behaviour in both language-only and multimodal models [20, 42, 55]. In addition, all experiments were performed with the temperature parameter set to zero, i.e., a deterministic setting with reduced sampling variability relative to higher-temperature decoding. We therefore interpret the low refusal rate as consistent with stronger task compliance under instruction-tuned, deterministic inference, although isolating this effect would require a dedicated ablation. Additionally, it is important to note that in this study, we didn't use cross-validation because of the time and resource constraints. We are aware that such an approach limits generalisation, but we made sure that the evaluation sets for both datasets were randomly selected and balanced.

In this study, we used CLIP as the embedding model for support-set retrieval. However, many other embedding models are available, including general-purpose models such as Gemini Embeddings 2 [19] and DINOv3 [64], as well as models fine-tuned on medical data, such as MedCLIP [74]

and BiomedCLIP [82]. These alternatives may be able to provide better representations of wound images, thereby improving both context-set retrieval and ICL performance. Because our focus was on SMLMs and their interaction with ICL, evaluating the impact of different embedding models was beyond the scope of this work and is left for future research. Additionally, we used SMLMs for ICL out of the box, without fine-tuning them on the task-specific datasets. Despite this, the larger models achieved higher accuracy than the fine-tuned supervised models, suggesting that task-specific fine-tuning could further improve SMLM performance [57, 86]. An investigation of the effects of fine-tuning on general performance and ICL is planned for our future work.

The deployment of AI models in clinical environments involves a range of considerations that extend beyond algorithmic performance. In healthcare, patient data are highly sensitive, which often restricts access to comprehensive datasets and imposes stringent privacy and security requirements. Consequently, models may need to operate locally rather than through cloud-based services, and their development must account for limited data availability, regulatory constraints, and the need for robust privacy-preserving mechanisms. The small multimodal language models evaluated in this study demonstrate considerable potential to meet the practical constraints of on-premises deployment in healthcare settings. The smallest variants, Qwen 3.5 0.8B, 2B, 4B, Ministral 3 3B, and Gemma 4 E2B, were the most straightforward to run locally and required modest computational resources. Mid-sized and larger models, including Qwen 3.5 9B and 27B, Ministral 3 8B and 14B, and Gemma 4 E4B and 26B A4B, also remained feasible on consumer-grade hardware, albeit with more careful optimisation.

Acknowledgments

The authors acknowledge the Swedish Knowledge Foundation, Jönköping University, and the industrial partners, including Mölnlycke Health Care, for financially supporting the research through the following project: ETIAI (Grant number 20230036), as part of the research and education environment SPARK at Jönköping University, Sweden.

Author contributions statement

G.M., O.G., J.P., and E.A. designed the study. G.M. conducted the experiments. G.M., O.G., J.P., and E.A. analysed the results. All authors contributed to the writing and reviewed the manuscript.

Declaration of generative AI and AI-assisted technologies in the manuscript preparation process

During the preparation of this work, the author(s) used OpenAI's GPT Image 2 in order to generate schematic wound images for Figure 1. These images were used only for visual illustration and were not included in the datasets, model inputs, evaluation sets, or experimental analyses. After using this tool/service, the author(s) reviewed and edited the content as needed and take(s) full responsibility for the content of the published article.

References

[1] Aliyu Abubakar, Hassan Ugail, and Ali Maina Bukar. Can machine learning be used to discriminate between burns and pressure ulcer? In *Proceedings of SAI intelligent systems conference*, pages 870–880. Springer, 2019.

[2] Divyansh Agarwal, Alexander R Fabbri, Ben Risher, Philippe Laban, Shafiq Joty, and Chien-Sheng Wu. Prompt leakage effect and defense strategies for multi-turn llm interactions. *arXiv preprint arXiv:2404.16251*, 2024.

[3] Ravi Aggarwal, Viknesh Sounderajah, Guy Martin, Daniel SW Ting, Alan Karthikesalingam, Dominic King, Hutan Ashrafian, and Ara Darzi. Diagnostic accuracy of deep learning in medical imaging: a systematic review and meta-analysis. *NPJ digital medicine*, 4(1):65, 2021.

[4] Jean-Baptiste Alayrac, Jeff Donahue, Pauline Luc, Antoine Miech, Iain Barr, Yana Hasson, Karel Lenc, Arthur Mensch, Katherine Millican, Malcolm Reynolds, et al. Flamingo: a visual language model for few-shot learning. *Advances in neural information processing systems*, 35:23716–23736, 2022.

[5] Zaid A Aldoulah, Hafiz Malik, and Richard Molyet. A novel fused multi-class deep learning approach for chronic wounds classification. *Applied Sciences*, 13(21):11630, 2023.

[6] D M Anisuzzaman, Behnoosh Rostami, Joseph Niezgoda, Ashwin Gopalakrishna, Zhihong Yu, and Zhiqiang Liang. Multi-modal wound classification using wound image and location by deep neural network. *Scientific Reports*, 12(1):17298, 2022.

[7] DM Anisuzzaman, Chuanbo Wang, Behrouz Rostami, Sandeep Gopalakrishnan, Jeffrey Niezgoda, and Zeyun Yu. Image-based artificial intelligence in wound assessment: a systematic review. *Advances in Wound Care*, 11(12):687–709, 2022.

[8] Murat S Ayhan, Ariel Y Ong, Eden Ruffell, Siegfried K Wagner, David A Merle, and Pearse A Keane. In-context learning for data-efficient diabetic retinopathy detection via multimodal foundation models. *Ophthalmology Science*, page 100934, 2025.

[9] Bobby Azad, Reza Azad, Sania Eskandari, Afshin Bozorgpour, Amirhossein Kazerouni, Islem Rekik, and Dorit Merhof. Foundational models in medical imaging: A comprehensive survey and future vision. *arXiv preprint arXiv:2310.18689*, 2023.

[10] Mohammed Baharoon, Waseem Qureshi, Jiahong Ouyang, Yanwu Xu, Abdulrhman Aljouie, and Wei Peng. Evaluating general purpose vision foundation models for medical image analysis: An experimental study of dinov2 on radiology benchmarks. *arXiv preprint arXiv:2312.02366*, 2023.

[11] Isabel Barbera. Ai privacy risks & mitigations–large language models (llms). *European Data Protection Board*, pages 2025–04, 2025.

[12] Yueyan Bian, Jin Li, Chuyang Ye, Xiuqin Jia, and Qi Yang. Artificial intelligence in medical imaging: from task-specific models to large-scale foundation models. *Chinese Medical Journal*, 138(06):651–663, 2025.

[13] Tabja Bortesi, Juan Pablo, Jonathan Ranisau, Shuang Di, Michael McGillion, Laura Rosella, Alistair Johnson, P. J. Devereaux, and Jeremy Petch. Machine learning approaches for the

image-based identification of surgical wound infections: Systematic review. *Journal of Medical Internet Research*, 26:e52880, 2024.

[14] Tyler J Bradshaw, Xin Tie, Joshua Warner, Junjie Hu, Quanzheng Li, and Xiang Li. Large language models and large multimodal models in medical imaging: a primer for physicians. *Journal of nuclear medicine*, 66(2):173–182, 2025.

[15] Tom Brown, Benjamin Mann, Nick Ryder, Melanie Subbiah, Jared D Kaplan, Prafulla Dhariwal, Arvind Neelakantan, Pranav Shyam, Girish Sastry, Amanda Askell, et al. Language models are few-shot learners. *Advances in neural information processing systems*, 33:1877–1901, 2020.

[16] Jaime Carbonell and Jade Goldstein. The use of mmr, diversity-based reranking for reordering documents and producing summaries. In *Proceedings of the 21st annual international ACM SIGIR conference on Research and development in information retrieval*, pages 335–336, 1998.

[17] Shuo Chen, Zhen Han, Bailan He, Jianzhe Liu, Mark Buckley, Yao Qin, Philip Torr, Volker Tresp, and Jindong Gu. Can multimodal large language models truly perform multimodal in-context learning? In *2025 IEEE/CVF Winter Conference on Applications of Computer Vision (WACV)*, pages 6000–6010. IEEE, 2025.

[18] Joon Yul Choi and Tae Keun Yoo. Evaluating chatgpt-4o for ophthalmic image interpretation: from in-context learning to code-free clinical tool generation. *Informatics and Health*, 2(2):158–169, 2025.

[19] Min Choi and Tom Duerig. Gemini embedding 2: Our first natively multimodal embedding model, Mar 2026. The Keyword Blog. Accessed: 2026-05-12.

[20] Hyung Won Chung, Le Hou, Shayne Longpre, Barret Zoph, Yi Tay, William Fedus, Yunxuan Li, Xuezhi Wang, Mostafa Dehghani, Siddhartha Brahma, et al. Scaling instruction-finetuned language models. *Journal of Machine Learning Research*, 25(70):1–53, 2024.

[21] Jacob Cohen. A coefficient of agreement for nominal scales. *Educational and psychological measurement*, 20(1):37–46, 1960.

[22] Tim Dettmers, Artidoro Pagnoni, Ari Holtzman, and Luke Zettlemoyer. Qlora: Efficient finetuning of quantized llms. *Advances in neural information processing systems*, 36:10088–10115, 2023.

[23] Qingxiu Dong, Lei Li, Damai Dai, Ce Zheng, Jingyuan Ma, Rui Li, Heming Xia, Jingjing Xu, Zhiyong Wu, Baobao Chang, et al. A survey on in-context learning. In *Proceedings of the 2024 conference on empirical methods in natural language processing*, pages 1107–1128, 2024.

[24] Alexey Dosovitskiy, Lucas Beyer, Alexander Kolesnikov, Dirk Weissenborn, Xiaohua Zhai, Thomas Unterthiner, Mostafa Dehghani, Matthias Minderer, Georg Heigold, Sylvain Gelly, Jakob Uszkoreit, and Neil Houlsby. An image is worth 16x16 words: Transformers for image recognition at scale. *arXiv preprint arXiv:2010.11929*, 2021.

[25] Sedigheh Eslami, Christoph Meinel, and Gerard De Melo. Pubmedclip: How much does clip benefit visual question answering in the medical domain? In *Findings of the Association for Computational Linguistics: EACL 2023*, pages 1181–1193, 2023.

[26] Dyke Ferber, Georg Wölflein, Isabella C Wiest, Marta Ligero, Srividhya Sainath, Narmin Ghaffari Laleh, Omar SM El Nahhas, Gustav Müller-Franzes, Dirk Jäger, Daniel Truhn, et al. In-context learning enables multimodal large language models to classify cancer pathology images. *Nature Communications*, 15(1):10104, 2024.

[27] Ronald Aylmer Fisher. Statistical methods for research workers. In *Breakthroughs in statistics: Methodology and distribution*, pages 66–70. Springer, 1970.

[28] Muskan Garg, Shaina Raza, Shebuti Rayana, Xingyi Liu, and Sunghwan Sohn. The rise of small language models in healthcare: A comprehensive survey. *arXiv preprint arXiv:2504.17119*, 2025.

[29] Gemma Team, Google DeepMind. Gemma 4: Our most capable open models to date. Google Blog, 2026. Accessed: 2026-04-15.

[30] Manu Goyal, Neil D Reeves, Satyan Rajbhandari, Naseer Ahmad, Chuan Wang, and Moi Hoon Yap. Recognition of ischaemia and infection in diabetic foot ulcers: Dataset and techniques. *Computers in biology and medicine*, 117:103616, 2020.

[31] Hao Guan and Mingxia Liu. Domain adaptation for medical image analysis: a survey. *IEEE Transactions on Biomedical Engineering*, 69(3):1173–1185, 2021.

[32] Kaiming He, Xiangyu Zhang, Shaoqing Ren, and Jian Sun. Deep residual learning for image recognition. In *Proceedings of the IEEE Conference on Computer Vision and Pattern Recognition*, pages 770–778, 2016.

[33] Jordan Hoffmann, Sebastian Borgeaud, Arthur Mensch, Elena Buchatskaya, Trevor Cai, Eliza Rutherford, DDL Casas, Lisa Anne Hendricks, Johannes Welbl, Aidan Clark, et al. Training compute-optimal large language models. *arXiv preprint arXiv:2203.15556*, 10, 2022.

[34] Edward J Hu, Yelong Shen, Phillip Wallis, Zeyuan Allen-Zhu, Yuanzhi Li, Shean Wang, Liang Wang, Weizhu Chen, et al. Lora: Low-rank adaptation of large language models. *Iclr*, 1(2):3, 2022.

[35] Yixing Jiang, Jeremy Irvin, Ji Hun Wang, Muhammad Ahmed Chaudhry, Jonathan H Chen, and Andrew Y Ng. Many-shot in-context learning in multimodal foundation models. *arXiv preprint arXiv:2405.09798*, 2024.

[36] Jared Kaplan, Sam McCandlish, Tom Henighan, Tom B Brown, Benjamin Chess, Rewon Child, Scott Gray, Alec Radford, Jeffrey Wu, and Dario Amodei. Scaling laws for neural language models. *arXiv preprint arXiv:2001.08361*, 2020.

[37] Janak Kapuriya, Manit Kaushik, Debasis Ganguly, and Sumit Bhatia. Exploring the role of diversity in example selection for in-context learning. In *Proceedings of the 48th International ACM SIGIR Conference on Research and Development in Information Retrieval*, pages 2962–2966, 2025.

[38] Bidur Khanal, SM Kamrul Hasan, Bishesh Khanal, and Cristian A Linte. Investigating the impact of class-dependent label noise in medical image classification. In *Proceedings of SPIE–the International Society for Optical Engineering*, volume 12464, page 1246437, 2023.

[39] Eugene Lee, Yu-Chi Lin, and Jiajie Diao. Learning to select visual in-context demonstrations. *arXiv preprint arXiv:2603.26775*, 2026.

[40] Junnan Li, Dongxu Li, Silvio Savarese, and Steven Hoi. Blip-2: Bootstrapping language-image pre-training with frozen image encoders and large language models. In *International conference on machine learning*, pages 19730–19742. PMLR, 2023.

[41] Li Li, Jiawei Peng, Huiyi Chen, Chongyang Gao, and Xu Yang. How to configure good in-context sequence for visual question answering. In *Proceedings of the IEEE/CVF Conference on Computer Vision and Pattern Recognition*, pages 26710–26720, 2024.

[42] Haotian Liu, Chunyuan Li, Qingyang Wu, and Yong Jae Lee. Visual instruction tuning. *Advances in neural information processing systems*, 36:34892–34916, 2023.

[43] Zhuang Liu, Hanzi Mao, Chao-Yuan Wu, Christoph Feichtenhofer, Trevor Darrell, and Saining Xie. A convnet for the 2020s. In *Proceedings of the IEEE/CVF Conference on Computer Vision and Pattern Recognition*, pages 11976–11986, 2022.

[44] Zhenyan Lu, Xiang Li, Dongqi Cai, Rongjie Yi, Fangming Liu, Xiwen Zhang, Nicholas D Lane, and Mengwei Xu. Small language models: Survey, measurements, and insights. *arXiv preprint arXiv:2409.15790*, 2024.

[45] Yang Luo, Zangwei Zheng, Zirui Zhu, and Yang You. How does the textual information affect the retrieval of multimodal in-context learning? In *Proceedings of the 2024 Conference on Empirical Methods in Natural Language Processing*, pages 5321–5335, 2024.

[46] Kenneth A McLean, Alessandro Sgrò, Leo R Brown, Louis F Buijs, Katie E Mountain, Catherine A Shaw, Thomas M Drake, Riinu Pius, Stephen R Knight, Cameron J Fairfield, et al. Multimodal machine learning to predict surgical site infection with healthcare workload impact assessment. *npj Digital Medicine*, 8(1):121, 2025.

[47] Quinn McNemar. Note on the sampling error of the difference between correlated proportions or percentages. *Psychometrika*, 12(2):153–157, 1947.

[48] Medline Industries. Arterial vs venous ulcers: What's the difference?, 2023. Accessed: 2026-06-27.

[49] Sewon Min, Xinxi Lyu, Ari Holtzman, Mikel Artetxe, Mike Lewis, Hannaneh Hajishirzi, and Luke Zettlemoyer. Rethinking the role of demonstrations: What makes in-context learning work? In *Proceedings of the 2022 conference on empirical methods in natural language processing*, pages 11048–11064, 2022.

[50] Mistral AI. Ministral 3. *arXiv preprint arXiv:2601.08584*, 2026.

[51] Michael Moor, Qian Huang, Shirley Wu, Michihiro Yasunaga, Yash Dalmia, Jure Leskovec, Cyril Zakka, Eduardo Pontes Reis, and Pranav Rajpurkar. Med-flamingo: a multimodal medical few-shot learner. In *Machine learning for health (ML4H)*, pages 353–367. PMLR, 2023.

[52] Yoojin Nam, Dong Yeong Kim, Sunggu Kyung, Jinyoung Seo, Jeong Min Song, Jimin Kwon, Jihyun Kim, Wooyoung Jo, Hyungbin Park, Jimin Sung, et al. Multimodal large language models in medical imaging: current state and future directions. *Korean Journal of Radiology*, 26(10):900, 2025.

[53] Harsha Nori, Yin Tat Lee, Sheng Zhang, Dean Carignan, Richard Edgar, Nicolo Fusi, Nicholas King, Jonathan Larson, Yuanzhi Li, Weishung Liu, et al. Can generalist foundation models outcompete special-purpose tuning? case study in medicine. *arXiv preprint arXiv:2311.16452*, 2023.

[54] Maxime Oquab, Timothée Darcet, Théo Moutakanni, Huy Vo, Marc Szafraniec, Vasil Khalidov, Pierre Fernandez, Daniel Haziza, Francisco Massa, Alaaeldin El-Nouby, et al. Dinov2: Learning robust visual features without supervision. *arXiv preprint arXiv:2304.07193*, 2023.

[55] Long Ouyang, Jeffrey Wu, Xu Jiang, Diogo Almeida, Carroll Wainwright, Pamela Mishkin, Chong Zhang, Sandhini Agarwal, Katarina Slama, Alex Ray, et al. Training language models to follow instructions with human feedback. *Advances in neural information processing systems*, 35:27730–27744, 2022.

[56] Yash Patel, Tirth Shah, Mrinal Kanti Dhar, Taiyu Zhang, Jeffrey Niezgoda, Sandeep Gopalakrishnan, and Zeyun Yu. Integrated image and location analysis for wound classification: a deep learning approach. *Scientific Reports*, 14(1):7043, 2024.

[57] Karmvir Singh Phogat, Sai Akhil Puranam, Sridhar Dasaratha, Chetan Harsha, and Shashishekar Ramakrishna. Fine-tuning smaller language models for question answering over financial documents. In *Findings of the Association for Computational Linguistics: EMNLP 2024*, pages 10528–10548, 2024.

[58] Qwen Team. Qwen3.5: Towards native multimodal agents, February 2026.

[59] Alec Radford, Jong Wook Kim, Chris Hallacy, Aditya Ramesh, Gabriel Goh, Sandhini Agarwal, Girish Sastry, Amanda Askell, Pamela Mishkin, Jack Clark, et al. Learning transferable visual models from natural language supervision. In *International conference on machine learning*, pages 8748–8763. PmLR, 2021.

[60] Dhanesh Ramachandram, Jose Luis Ramirez-GarciaLuna, Robert DJ Fraser, Mario Aurelio Martínez-Jiménez, Jesus E Arriaga-Caballero, and Justin Allport. Fully automated wound tissue segmentation using deep learning on mobile devices: Cohort study. *JMIR mHealth and uHealth*, 10(4):e36977, 2022.

[61] Behrouz Rostami, DM Anisuzzaman, Chuanbo Wang, Sandeep Gopalakrishnan, Jeffrey Niezgoda, and Zeyun Yu. Multiclass wound image classification using an ensemble deep cnn-based classifier. *Computers in Biology and Medicine*, 134:104536, 2021.

[62] Gaetano Scebba, Jia Zhang, Sabrina Catanzaro, Carina Mihai, Oliver Distler, Martin Berli, and Walter Karlen. Detect-and-segment: A deep learning approach to automate wound image segmentation. *Informatics in Medicine Unlocked*, 29:100884, 2022.

[63] Mobina Shrestha, Bishwas Mandal, Vishal Mandal, Asis Shrestha, and Amir Babu Shrestha. In-context learning for label-efficient cancer image classification in oncology. *Informatics in Medicine Unlocked*, page 101683, 2025.

[64] Oriane Siméoni, Huy V Vo, Maximilian Seitzer, Federico Baldassarre, Maxime Oquab, Cijo Jose, Vasil Khalidov, Marc Szafraniec, Seungeun Yi, Michaël Ramamonjisoa, et al. Dinov3. *arXiv preprint arXiv:2508.10104*, 2025.

[65] Kai Sun, Siyan Xue, Fuchun Sun, Haoran Sun, Yu Luo, Ling Wang, Siyuan Wang, Na Guo, Lei Liu, Tian Zhao, et al. Medical multimodal foundation models in clinical diagnosis and treatment: Applications, challenges, and future directions. *Artificial Intelligence in Medicine*, page 103265, 2025.

[66] Yiyao Sun, Xinran Wen, Yan Zhang, Lijun Jin, Chunna Yang, Qianhui Zhang, Mingchen Jiang, Zhaoyang Xu, Wei Guo, Juan Su, et al. Visual-language foundation models in medical imaging: A systematic review and meta-analysis of diagnostic and analytical applications. *Computer Methods and Programs in Biomedicine*, 268:108870, 2025.

[67] Wei Suo, Lanqing Lai, Mengyang Sun, Hanwang Zhang, Peng Wang, and Yanning Zhang. Visual prompt selection for in-context learning segmentation. *arXiv preprint arXiv:2407.10233*, 2024.

[68] Mingxing Tan and Quoc V Le. Efficientnetv2: Smaller models and faster training. *arXiv preprint arXiv:2104.00298*, 2021.

[69] Maria Tsimpoukelli, Jacob L Menick, Serkan Cabi, SM Eslami, Oriol Vinyals, and Felix Hill. Multimodal few-shot learning with frozen language models. *Advances in Neural Information Processing Systems*, 34:200–212, 2021.

[70] Chien Van Nguyen, Xuan Shen, Ryan Aponte, Yu Xia, Samyadeep Basu, Zhengmian Hu, Jian Chen, Mihir Parmar, Sasidhar Kunapuli, Joe Barrow, et al. A survey on small language models. In *Proceedings of the 15th International Conference on Recent Advances in Natural Language Processing-Natural Language Processing in the Generative AI Era*, pages 807–821, 2025.

[71] Changhan Wang, Xinchen Yan, Max Smith, Kanika Kochhar, Marcie Rubin, Stephen M Warren, James Wrobel, and Honglak Lee. A unified framework for automatic wound segmentation and analysis with deep convolutional neural networks. In *2015 37th annual international conference of the ieee engineering in medicine and biology society (EMBC)*, pages 2415–2418. IEEE, 2015.

[72] Chuanbo Wang, DM Anisuzzaman, Victor Williamson, Mrinal Kanti Dhar, Behrouz Rostami, Jeffrey Niezgoda, Sandeep Gopalakrishnan, and Zeyun Yu. Fully automatic wound segmentation with deep convolutional neural networks. *Scientific reports*, 10(1):21897, 2020.

[73] Haoran Wang, Qiuye Jin, Shiman Li, Siyu Liu, Manning Wang, and Zhijian Song. A comprehensive survey on deep active learning in medical image analysis. *Medical Image Analysis*, 95:103201, 2024.

[74] Zifeng Wang, Zhenbang Wu, Dinesh Agarwal, and Jimeng Sun. Medclip: Contrastive learning from unpaired medical images and text. In *Proceedings of the 2022 Conference on Empirical Methods in Natural Language Processing*, pages 3876–3887, 2022.

[75] Yishu Wei, Yu Deng, Cong Sun, Mingquan Lin, Hongmei Jiang, and Yifan Peng. Deep learning with noisy labels in medical prediction problems: a scoping review. *Journal of the American Medical Informatics Association*, 31(7):1596–1607, 2024.

[76] Jin-Ming Wu, Chia-Jui Tsai, Te-Wei Ho, Feipei Lai, Hao-Chih Tai, and Ming-Tsan Lin. A unified framework for automatic detection of wound infection with artificial intelligence. *Applied Sciences*, 10(15):5353, 2020.

[77] Guangzhi Xiong, Sanchit Sinha, Zhenghao He, and Aidong Zhang. Retrieving counterfactuals improves visual in-context learning. *arXiv preprint arXiv:2603.16737*, 2026.

[78] Jiajun Xu, Zhiyuan Li, Wei Chen, Qun Wang, Xin Gao, Qi Cai, and Ziyuan Ling. On-device language models: A comprehensive review. *arXiv preprint arXiv:2409.00088*, 2024.

[79] DP Yadav, Ashish Sharma, Madhusudan Singh, and Ayush Goyal. Feature extraction based machine learning for human burn diagnosis from burn images. *IEEE journal of translational engineering in health and medicine*, 7:1–7, 2019.

[80] Ruyi Zhang, Dingcheng Tian, Dechao Xu, Wei Qian, and Yudong Yao. A survey of wound image analysis using deep learning: classification, detection, and segmentation. *IEEE Access*, 10:79502–79515, 2022.

[81] Shaoting Zhang and Dimitris Metaxas. On the challenges and perspectives of foundation models for medical image analysis. *Medical image analysis*, 91:102996, 2024.

[82] Sheng Zhang, Yanbo Xu, Naoto Usuyama, Hanwen Xu, Jaspreet Bagga, Robert Tinn, Sam Preston, Rajesh Rao, Mu Wei, Naveen Valluri, et al. Biomedclip: a multimodal biomedical foundation model pretrained from fifteen million scientific image-text pairs. *arXiv preprint arXiv:2303.00915*, 2023.

[83] Yuanhan Zhang, Kaiyang Zhou, and Ziwei Liu. What makes good examples for visual in-context learning? *Advances in Neural Information Processing Systems*, 36:17773–17794, 2023.

[84] Zihao Zhao, Eric Wallace, Shi Feng, Dan Klein, and Sameer Singh. Calibrate before use: Improving few-shot performance of language models. In *International conference on machine learning*, pages 12697–12706. Pmlr, 2021.

[85] Xiaoying Zhong, Siyi Li, Zhao Chen, Long Ge, Dongdong Yu, Shijia Wang, Liangzhen You, and Hongcai Shang. Considerations for patient privacy of large language models in health care: scoping review. *Journal of Medical Internet Research*, 27:e76571, 2025.

[86] Xiongtao Zhou, Jie He, Yuhua Ke, Guangyao Zhu, Víctor Gutiérrez-Basulto, and Jeff Pan. An empirical study on parameter-efficient fine-tuning for multimodal large language models. In *Findings of the Association for Computational Linguistics: ACL 2024*, pages 10057–10084, 2024.

A Retrieval-control association statistics

To complement the paired retrieval-control comparisons, we report conditional correctness and association statistics for each model–control comparison for both Kaggle and Medetec datasets. For each paired 2×2 correctness table, we computed the retention rate, $P(\text{SMLM correct} \mid \text{control correct})$, the rescue rate, $P(\text{SMLM correct} \mid \text{control wrong})$, Fisher's exact test p-value, and the corresponding odds ratio (OR).

Table 10: Conditional correctness and association statistics for kNN few-shot prompting relative to the global weighted-kNN control in the Kaggle dataset. Ret. denotes $P(\text{SMLM correct} \mid \text{control correct})$, Resc. denotes $P(\text{SMLM correct} \mid \text{control wrong})$, Fisher p is the exact Fisher test p-value, and OR denotes the corresponding odds ratio.

Model	**Ret.**	**Resc.**	**Fisher p**	**OR**
Gemma 4 26B A4B	0.966	0.630	1.81×10^{-11}	16.73
Qwen 3.5 27B	0.960	0.616	1.86×10^{-11}	15.11
Qwen 3.5 9B	0.938	0.589	1.56×10^{-10}	10.53
Qwen 3.5 4B	0.921	0.438	1.11×10^{-15}	14.92
Ministral 3 14B	0.881	0.438	1.36×10^{-12}	9.52
Gemma 4 E4B	0.876	0.397	5.10×10^{-14}	10.69
Qwen 3.5 2B	0.853	0.342	5.18×10^{-15}	11.15
Ministral 3 8B	0.785	0.342	6.66×10^{-11}	7.02
Ministral 3 3B	0.633	0.342	4.26×10^{-5}	3.31
Gemma 4 E2B	0.520	0.301	0.002	2.51
Qwen 3.5 0.8B	0.362	0.247	0.103	1.73

Table 11: Conditional correctness and association statistics for kNN+MMR few-shot prompting relative to the matched weighted-kNN control recomputed on the final reranked support set in the Kaggle dataset. Ret. denotes $P(\text{SMLM correct} \mid \text{control correct})$, Resc. denotes $P(\text{SMLM correct} \mid \text{control wrong})$, Fisher p is the exact Fisher test p-value, and OR denotes the corresponding odds ratio.

Model	**Ret.**	**Resc.**	**Fisher p**	**OR**
Gemma 4 26B A4B	0.941	0.629	1.17×10^{-8}	9.49
Qwen 3.5 27B	0.936	0.645	1.01×10^{-7}	8.07
Qwen 3.5 9B	0.926	0.694	1.45×10^{-5}	5.49
Qwen 3.5 4B	0.904	0.435	2.33×10^{-13}	12.24
Qwen 3.5 2B	0.856	0.419	6.80×10^{-11}	8.26
Ministral 3 14B	0.814	0.387	1.11×10^{-9}	6.92
Ministral 3 8B	0.761	0.339	3.76×10^{-9}	6.20
Gemma 4 E4B	0.851	0.306	2.55×10^{-15}	12.93
Ministral 3 3B	0.654	0.355	5.12×10^{-5}	3.44
Gemma 4 E2B	0.484	0.323	0.028	1.97
Qwen 3.5 0.8B	0.340	0.177	0.016	2.39

Table 12: Conditional correctness and association statistics for kNN few-shot prompting relative to the global weighted-kNN control in the Medetec dataset. Ret. denotes P(SMLM correct | control correct), Resc. denotes P(SMLM correct | control wrong), Fisher p is the exact Fisher test p-value, and OR denotes the corresponding odds ratio.

Model	**Ret.**	**Resc.**	**Fisher p**	**OR**
Qwen 3.5 27B	0.952	0.354	9.35×10^{-10}	36.47
Qwen 3.5 9B	0.857	0.375	3.71×10^{-6}	10.00
Gemma 4 26B A4B	0.810	0.354	1.61×10^{-5}	7.75
Qwen 3.5 4B	0.810	0.375	3.93×10^{-5}	7.08
Ministral 3 14B	0.714	0.312	2.79×10^{-4}	5.50
Gemma 4 E4B	0.905	0.208	9.60×10^{-12}	36.10
Qwen 3.5 2B	0.714	0.375	0.002	4.17
Ministral 3 8B	0.690	0.229	1.60×10^{-5}	7.50
Gemma 4 E2B	0.524	0.229	0.005	3.70
Ministral 3 3B	0.476	0.188	0.006	3.94
Qwen 3.5 0.8B	0.214	0.271	0.626	0.73

Table 13: Conditional correctness and association statistics for kNN+MMR few-shot prompting relative to the matched weighted-kNN control recomputed on the final reranked support set in the Medetec dataset. Ret. denotes P(SMLM correct | control correct), Resc. denotes P(SMLM correct | control wrong), Fisher p is the exact Fisher test p-value, and OR denotes the corresponding odds ratio.

Model	**Ret.**	**Resc.**	**Fisher p**	**OR**
Qwen 3.5 27B	0.976	0.429	8.58×10^{-9}	53.33
Qwen 3.5 9B	0.951	0.327	2.70×10^{-10}	40.22
Gemma 4 26B A4B	0.878	0.388	1.50×10^{-6}	11.37
Qwen 3.5 4B	0.829	0.449	2.20×10^{-4}	5.96
Ministral 3 14B	0.805	0.245	1.83×10^{-7}	12.72
Gemma 4 E4B	0.854	0.224	1.45×10^{-9}	20.15
Qwen 3.5 2B	0.780	0.388	2.49×10^{-4}	5.61
Ministral 3 8B	0.756	0.204	1.81×10^{-7}	12.09
Ministral 3 3B	0.610	0.204	1.00×10^{-4}	6.09
Gemma 4 E2B	0.463	0.143	0.001	5.18
Qwen 3.5 0.8B	0.220	0.184	0.793	1.25

B Detailed kNN+MMR retrieval-control results

This appendix reports the full paired retrieval-control results for the kNN+MMR prompting condition. These results are discussed only briefly in Section 4.2 because the diagnostic logic is identical to the primary kNN analysis in the main text.

Table 14: Paired retrieval-control comparisons for kNN+MMR few-shot prompting against the matched weighted-kNN control recomputed on the final reranked support set (accuracy = 0.752) on the Kaggle dataset. Top-1, Maj., and Any denote match rates to the top retrieved support label, the support-majority label, and any label present in the retrieved support set, respectively. Ret. denotes P(SMLM correct | control correct), and Resc. denotes P(SMLM correct | control wrong). Agreement denotes the raw prediction agreement rate with the control, and κ denotes Cohen's kappa.

Model	**Acc.**	**Δ**	**McNemar p**	**Top-1**	**Maj.**	**Any**	**Ret.**	**Resc.**	**Agreement**	κ
Qwen 3.5 9B	0.868	+0.116	< 0.001	0.704	0.756	0.972	0.926	0.694	0.744	0.715
Qwen 3.5 27B	0.864	+0.112	< 0.001	0.700	0.768	0.984	0.936	0.645	0.760	0.733
Gemma 4 26B A4B	0.864	+0.112	< 0.001	0.692	0.764	0.984	0.941	0.629	0.752	0.724
Qwen 3.5 4B	0.788	+0.036	0.233	0.680	0.768	0.984	0.904	0.435	0.768	0.741
Qwen 3.5 2B	0.748	-0.004	1.000	0.708	0.740	0.948	0.856	0.419	0.736	0.705
Ministral 3 14B	0.708	-0.044	0.193	0.640	0.688	0.920	0.814	0.387	0.672	0.634
Ministral 3 8B	0.656	-0.096	0.004	0.632	0.648	0.916	0.761	0.339	0.644	0.602
Gemma 4 E4B	0.716	-0.036	0.243	0.684	0.736	0.972	0.851	0.306	0.724	0.691
Ministral 3 3B	0.580	-0.172	< 0.001	0.540	0.548	0.820	0.654	0.355	0.536	0.484
Gemma 4 E2B	0.444	-0.308	< 0.001	0.396	0.408	0.668	0.484	0.323	0.400	0.332
Qwen 3.5 0.8B	0.300	-0.452	< 0.001	0.284	0.292	0.636	0.340	0.177	0.292	0.205

Table 15: Paired retrieval-control comparisons for kNN+MMR few-shot prompting against the matched weighted-kNN control recomputed on the final reranked support set (control accuracy = 0.456) on the Medetec dataset. Top-1, Maj., and Any denote match rates to the top retrieved support label, the support-majority label, and any label present in the retrieved support set, respectively. Ret. denotes P(SMLM correct | control correct), and Resc. denotes P(SMLM correct | control wrong). Agreement denotes the raw prediction agreement rate with the control, and κ denotes Cohen's kappa.

Model	**Acc.**	**Δ**	**McNemar p**	**Top-1**	**Maj.**	**Any**	**Ret.**	**Resc.**	**Agreement**	κ
Qwen 3.5 27B	0.678	+0.222	< 0.001	0.600	0.667	0.956	0.976	0.429	0.667	0.589
Qwen 3.5 9B	0.611	+0.156	0.001	0.522	0.589	0.978	0.951	0.327	0.589	0.522
Gemma 4 26B A4B	0.611	+0.156	0.007	0.522	0.567	0.933	0.878	0.388	0.567	0.488
Qwen 3.5 4B	0.622	+0.167	0.008	0.411	0.500	0.844	0.829	0.449	0.500	0.419
Ministral 3 14B	0.500	+0.044	0.503	0.533	0.578	0.967	0.805	0.245	0.578	0.492
Gemma 4 E4B	0.511	+0.056	0.332	0.511	0.600	0.933	0.854	0.224	0.600	0.505
Qwen 3.5 2B	0.567	+0.111	0.087	0.456	0.433	0.911	0.780	0.388	0.433	0.379
Ministral 3 8B	0.456	+0.000	1.000	0.522	0.511	0.856	0.756	0.204	0.511	0.411
Ministral 3 3B	0.389	-0.067	0.327	0.300	0.356	0.767	0.610	0.204	0.356	0.290
Gemma 4 E2B	0.289	-0.167	0.008	0.333	0.278	0.844	0.463	0.143	0.267	0.178
Qwen 3.5 0.8B	0.200	-0.256	< 0.001	0.167	0.111	0.433	0.220	0.184	0.111	0.060